# University Politehnica of Bucharest

Doctoral School of Energy Engineering

Faculty of Energy Engineering

Department of Hydraulics, Hydraulic machinery and Environmental Engineering
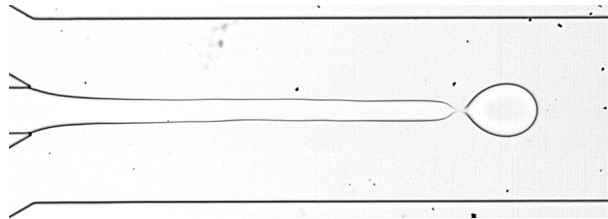
REOROM Laboratory

Decision no. ... of ../../....

## PHD THESIS

# The study of interfaces in microchannels under the influence of external fields.



## Author: PhD Student eng. Eugen Chiriac

## Advisor: Prof. dr. eng. Corneliu Bălan

The doctoral committee

| Chairman | Prof. Dr. Eng. Radu Porumb | from | University Politehnica of Bucharest |
|---|---|---|---|
| Referee | S.R.I. Dr. Marioara Avram | from | NI for R&D in Microtechnologies - IMT Bucharest |
| Referee | Prof. Dr. Eng. Ilinca Năstase | from | Technical University of Civil Engineering Bucharest |
| Advisor | Prof. Dr. Eng. Corneliu Bălan | from | University Politehnica of Bucharest |
| Referee | Prof. Dr. Eng. Diana Broboană | from | University Politehnica of Bucharest |

BUCHAREST

2023

# Abstract

Graphical abstract
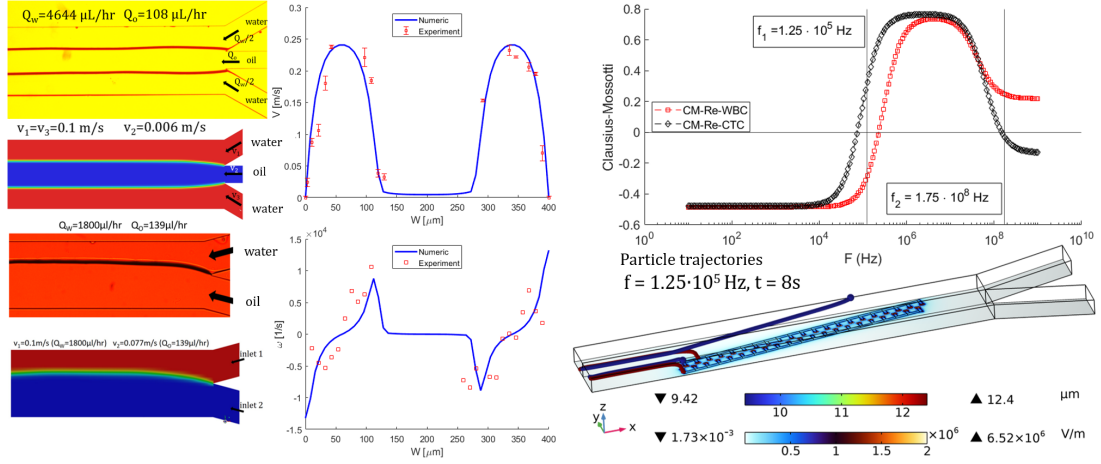
The thesis contributes to the understanding of interfacial phenomena occurring in microfluidic devices at the contact between two immiscible liquids, where the reduced dimensional aspect of the devices generates flow stability. Flow stability enables the investigation and modeling of the interface between two immiscible fluids in detail until the onset of instabilities.

The first part of the thesis introduces the fundamental theoretical aspects underlying fluid flow in microchannels. The numerical calculation method was presented for multiphase flow in the absence of phase diffusion.

The second part of the thesis presents the microchannel fabrication methods. The technological flow used for creating microfluidic devices used in this thesis was presented.

The third part of the thesis contains the developed applications based on investigated microfluidic configurations. The applications start with the study of laminar flow, continue with investigations of flow with immiscible fluids and conclude with experimental and numerical investigations of the influence of the external field on the interface of separation between two immiscible fluids.

In the final part of the thesis, passive and active methods for separating cells and particles in microfluidic configurations were presented. In this regard, two Lab-on-a-chip devices were created to separate red blood cells from circulating tumor cells in an alternative electric field using dielectrophoresis.

**Keywords:** microfluidics, interfacial flows, interface, CFD, Hele-Shaw microchannel, dielectrophoresis.

# Contents

# List of publications

**I. ISI articles published in international journals and reviewed**

- ROMJIST 2021 - Chiriac, E., Avram, M., & Bălan, C. (2021). Manipulation of particles using dielectrophoresis in a microchannel. *Rom. J. Inf. Sci. Technol*, 24, 213-221. IF: 0.852

- MICROMACHINES 2022 - Chiriac, E., Avram, M., & Balan, C. (2022). Investigation of Multiphase Flow in a Trifurcation Microchannel—A Benchmark Problem. *Micromachines*, 13(6), 974. IF: 3.523

- UPB 2022 - Chiriac, E., Avram, M., & Balan, C. (2022). Experimental and numerical investigation of hysteresis in multiphase flow in a microchannel. *U.P.B. Sci. Bull., Series A*, 84(3), 191-200. IF: 1.16

- Materials Today Communication - Burinaru, T. A., Adiaconiţă, B., Avram, M., Preda, P., Enciu, A. M., Chiriac, E., Marculescu, C., Constantin, T. & Militaru, M. (2022). Electrochemical impedance spectroscopy based microfluidic biosensor for the detection of circulating tumor cells. Materials Today Communications, 32, 104016. IF: 3.662

- Micromachines 2022 - Tincu, B., Burinaru, T., Enciu, A. M., Preda, P., Chiriac, E., Marculescu, C., Avram, M. & Avram, A. (2022). Vertical Graphene-Based Biosensor for Tumor Cell Dielectric Signature Evaluation. Micromachines, 13(10), 1671. IF: 3.523

**II. Web Of Science Publications and BDI**

- ATEE 2019 - Chiriac, E., Broboana, D., Avram, M., & Balan, C. (2019, March). Comparative numerical study between OpenFOAM and ANSYS Fluent in a Y-junction microchannel. *In 2019 11th International Symposium on Advanced Topics in Electrical Engineering (ATEE)* (pp. 1-4). IEEE.

- CIEM 2019 - Chiriac, E., Avram, M., Broboana, D., & Balan, C. (2019, October). Interface Evolution in a Microchannel, an Experimental and Numerical Study. *In 2019 International Conference on ENERGY and ENVIRONMENT (CIEM)* (pp. 219-223). IEEE.

- CAS 2020 - Chiriac, E., Avram, M., & Bălan, C. (2020, October). Dielectrophoretic separation of Circulating Tumor Cells and Red Blood Cells in a microfluidic device. *In 2020 International Semiconductor Conference (CAS)* (pp. 211-214). IEEE.

- EENVIRO 2020 - Chiriac, E., Bratu, A. M., Avram, M., & Bălan, C. (2021, May). Alcohol jets investigations in a microchannel in a viscous outer medium. *In IOP Conference Series: Earth and Environmental Science* (Vol. 664, No. 1, p. 012056). IOP Publishing.

- ATEE 2021 - Chiriac, E., Bran, A. M., Voitincu, C., & Balan, C. (2021, March). Experimental validation of VOF method in microchannel flows. *In 2021 12th International Symposium on Advanced Topics in Electrical Engineering (ATEE)* (pp. 1-4). IEEE.

- CIEM 2021 Chiriac, E., Avram, M., & Balan, C. (2021, October). Transition from Threads to Droplets in a Microchannel for Liquids with No Viscosity Contrast. *In 2021 10th International Conference on ENERGY and ENVIRONMENT (CIEM)* (pp. 1-4). IEEE.

- CAS 2021 Chiriac, E., Adiaconiță, B., Pachiu, C., Avram, M., & Bălan, C. (2021, October). MicroPIV on carbonic materials embedded in a microfluidic device. *In 2021 International Semiconductor Conference (CAS)* (pp. 169-172). IEEE.

- CAS 2022 Adiaconiță, B., Preda, P., Burinaru, T., Mărculescu, C., Avram, A., Crăciun, G., Chiriac, E., Avram, M. (2022, October). Electrochemical Biosensing Based on Graphene for Detection of the SARS-CoV-2 Nucleocapsid Protein. *In 2022 International Semiconductor Conference (CAS)*. IEEE.

- CAS 2022 Preda, P., Adiaconita, B., Craciun, G., Mihalache, I., Boldeiu, A., Brincoveanu, O., Maxim, M.-E., Chiriac, E., Avram, M., (2022, October). Chitosan-coated gold nanocomposites loading with cisplatin for potential use in cancer therapy. *In 2022 International Semiconductor Conference (CAS)*. IEEE.

### III. Participare cu lucrări științifice la conferințe internaționale

- 11th International Symposium on Advanced Topics in Electrical Engineering (ATEE) 2019

- International Conference on ENERGY and ENVIRONMENT (CIEM) 2019

- International Semiconductor Conference (CAS) 2020

- Conference of the Sustainable Solutions for Energy and Environment (EENVIRO) 2020

- 12th International Symposium on Advanced Topics in Electrical Engineering (ATEE) 2021

- 10th International Conference on ENERGY and ENVIRONMENT (CIEM) 2021

- International Semiconductor Conference (CAS) 2021

- International Conference on Rheology 2022

- International Semiconductor Conference (CAS) 2022

### IV. Membru în proiecte de cercetare

- Microfluidic platform for circulating tumour cells (CTCs) concentration through dielectrophoresis-magnetophoresis and analyzed via broadband dielectric spectroscopy and electrochemical impedance (PN-III-P1-1.2-PCCDI-2017-0214).

- Innovative approaches in the treatment and control of patients infected with SARS-CoV-2 virus (PN-III-P2-2.1-SOL-2020-0061).

- Magnetoresistive sensors optimized for on-chip detection of magnetic nanoparticles (PN-III-P2-2.1-PED-2019-3514).

- Combined CD36 immunoaffinity and nanostructure technology for metastatic tumor cells enrichment from blood (PN-III-P2-2.1-PED-2019-3141).

- Multi-disciplinary Use Cases for Convergent new Approaches to AI explainability (COFUND-CHIST ERA-MUCCA).

- Impedimetric biosensor based on vertical graphene, integrated with a microfluidic system for monitoring the plasma levels of anti-tumoral agents (PN-III-P2-2.1-PTE-2021-0444).

- Graphene based spintronic structures for sensing applications and signal processing (PN-III-P2-2.1-PED-2021-3112).

- Electrochemical microsensors for the detection of narcotics: codeine and morphine, Contract C77/9D, cod SMIS 2014+ 105623.

- Microfluidic platforms for biochemical sensors with applications in societal security, Contract C77/1C, cod SMIS 2014+ 105623.

# Extended abstract

## Introduction

Consider a microfluidic device with a bifurcation, connected to two pressure/flow pumps through which two incompressible and immiscible Newtonian fluids with different material properties are introduced into the device at different controlled inlet pressures/flow rates. The aim of the experimental procedure is to develop a separation interface between the two fluids. The position of the interface in the microchannel with defined geometry depends on the following factors: inlet pressures/flow rates, material properties of the two fluids, properties of the interfaces and the behavior of the fluids at the channel wall. The study of the interface is a central topic in microfluidics, with many applications based on multiphase flows associated with the transition between different flow regimes.

The present work is devoted to the study of the fluid interface in a microchannel with three inlets and one outlet, with applications in dielectrophoresis.

## Microfluidics

The global trend to miniaturize the components of dynamic systems has led to the development of devices such as Lab-on-a-Chip [51], Organ-on-a-Chip [3], devices with multidisciplinary applications incorporating elements of physics, chemistry, biology and engineering. Most applications require the transport of working fluids in microfluidic configurations. The transport of solutions through microfluidic devices occurs in the laminar flow regime, with geometry being of significant importance in the development of applications.

Lately, Lab-on-a-Chip devices and related applications are integrating artificial intelligence-related procedures. This helps to process the large volumes of data resulting from experiments. Initially machine learning is trained with the experimental data using an application-specific algorithm. For example, the CNN (Convolutional Neural Networks) algorithm is used on a wide range of applications such as cell isolation, cell sorting and flow cytometry and combined applications [51]. Once the learning machine is trained, it can analyze the dataset resulting from the experiment without further processing.

In energy, microfluidics is found in several applications [41]. In solar energy, microfluidic devices are used for photocatalysis [1] and photosynthesis [35]; they are also embedded in devices for electrochemical energy conversion, fuel cell storage and batteries. In [28] a microfluidic fuel cell with porous electrodes for electrochemical energy conversion has been developed. In [46] a microfluidic device with galvanic cells (called fluid batteries, integrated directly into the paper microchannel) that can light an LED is shown. In the oil and gas industry, microchannels play an important role by studying oil-in-water emulsions. In [19] a *Lab-on-a-Chip* device is used to study emulsion formation and recovery of heavy oil. Schematic presentation of the principle of operation as well as the resulting emulsions are shown in Fig. 1 I. In [32] the classical pressure-volume-temperature cell is replicated in miniature, in a microfluidic channel with coils and section narrowings, and used to measure fluid phase dynamics, Fig. 1 II. Microfluidics is

currently applied to carbon management as follows: in [27] $CO_2$ transport and salt formation dynamics are studied and in [43] the dew point of $CO_2$ with impurities was determined.
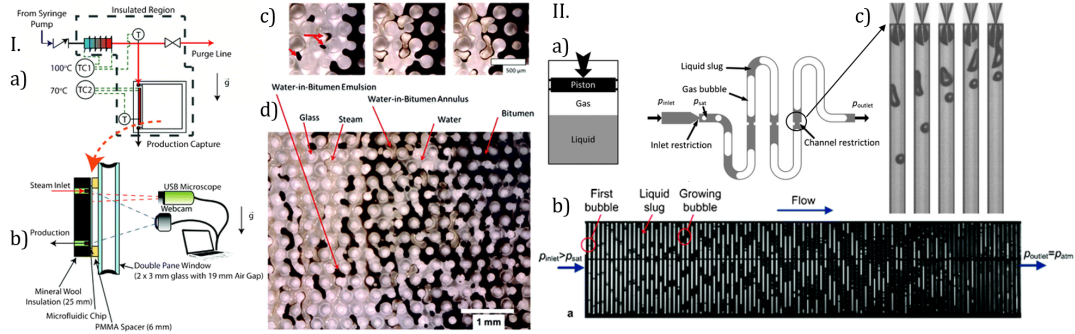


Figure 1: I. a) Schematic representation of the system creating bitumen-in-water emulsions, b) Acquisition system, c) Detail of bitumen-in-water emulsions, d) Overview of the whole SAGD process (*Steam Assisted Gravity Drainage*), Reprinted with permission from [19] ©(2013) Royal Society of Chemistry; II. a) Conventional techniques for measuring gas dynamics consisting of a high-pressure cylinder and piston and the microfluidic technique used to measure phase behaviour, b) Formation of multiphase flow, c) Detail of section narrowing with bubble formation ($p_{inlet} = 35\,bar$), Reprinted with permission from [32] ©(2012) Royal Society of Chemistry.

## Aim and motivation

In applied microfluidics most flows are multiphase, which justifies the experimental and numerical study of the evolution of interfaces in microchannels under the influence of external fields. An objective of this thesis is to establish benchmark problems in microfluidics, the so-called *benchmark problems*, for low dimensional ratio geometries:

- a microchannel with three inlets and one outlet, with a depth of $h = 50\,\mu m$ and a main channel width of $W = 400\,\mu m$;

- a bifurcated microchannel with a 30°textdegree angle between the two branches, with a depth of $h = 50\,\mu m$ and a main channel width of $W = 200\,\mu m$.

The aim is to validate qualitatively and quantitatively the numerical simulations, allowing the extension of the numerical studies with other geometries, configurations and non-Newtonian fluids. The influence of nanostructures on flow is also investigated. This allows the evaluation of technological processes used in the fabrication of microfluidic devices.

Another objective of the study is to investigate multiphase flows in order to evaluate the effect of external fields on flow and on the hysteresis phenomenon observed in flow dynamics.

The applied objective of the thesis is to develop Lab-on-a-Chip devices that allow the manipulation of particle trajectories using the dielectrophoretic force, in numerical simulations the particles are considered to have an ideal spherical shape.

## Theoretical aspects

### Navier-Stokes

Microfluidics is a branch of fluid mechanics in which flow takes place at small spatial scales, usually on the order of tens and hundreds of microns. This is reflected by the fact that the importance of inertial forces is reduced, with flow being dominated by viscous frictional forces, pressure forces and interfacial forces (if any). Also, the flow regime is laminar, the

turbulent regime being characteristic only of 3D geometries with extreme direction changes at small angles that facilitate mixing between fluid layers [44].

The isothermal flow of an incompressible, Newtonian (isoviscous) fluid is described by the Navier-Stokes system of equations, consisting of the momentum conservation equation (1) and the mass conservation equation (2):

$$\rho \left( \frac{\partial \mathbf{v}}{\partial t} + (\mathbf{v} \cdot \nabla) \, \mathbf{v} \right) = \rho \mathbf{b} - \nabla p + \eta \Delta \mathbf{v}, \tag{1}$$

$$div \, \mathbf{v} = 0, \tag{2}$$

where, $\mathbf{v}$ is the velocity vector, $\rho$ and $\eta$ are the material properties, density and viscosity respectively, $\mathbf{b}$ is the mass force and $p$ is the pressure. The unknowns of the system are the velocity $\mathbf{v}$ and the pressure $p$.

The relations (1) and (2), complete with the corresponding boundary and initial conditions, are valid for homogeneous and isotropic fluid. Typically, the solution of the Navier-Stokes equation is done numerically using specialized CFD (Computational Fluid Dynamics) codes implemented in commercial ANSYS or COMSOL software, OpenFOAM open-source software or custom closed-loop [4] software.

The present work is focused on the study of viscous flows in microchannels in the presence of an interface separating two immiscible fluids in the absence of diffusion. The model used considers that the equations (1) and (2) are valid in the whole flow domain occupied by the two fluids, the material functions (density and viscosity) being customized for each fluid by means of a function defining the interface. Thus, in the Navier-Stokes equation an additional term will appear, a specific force acting exclusively on the interface and depending on the interfacial tension between the two fluids.

## Fluid interface; VOF method

The Navier-Stokes equations (1) and (2) are second-order, nonlinear, partial-derivative equations. They represent the local (differential) form of the principles of conservation of mass and momentum, stated in integral form [6, 26].

The transition from integral to local form implies the continuity of unknown functions (velocity and pressure) and material functions/constants (density and viscosity).

If there are two immiscible, homogeneous and incompressible fluids separated by an interface in the flow domain, an additional term, a specific force acting exclusively on the interface, will have to be introduced into the Navier-Stokes equation. In this paragraph we present the procedure for implementing the specific force in the equation of motion (1).

In Fig. 2 the interface between two immiscible fluids is shown, where $S$ is the surface that is bounded on the interface surface $f(\mathbf{x}, t) = 0$ by the curve $C$, $\mathbf{v_s}$ is the interface velocity, $r_1$ and $r_2$ are the radii of curvature at $S$, $\mathbf{F_c}$ is the capillary force, $\sigma [N/m]$ is the interfacial tension.
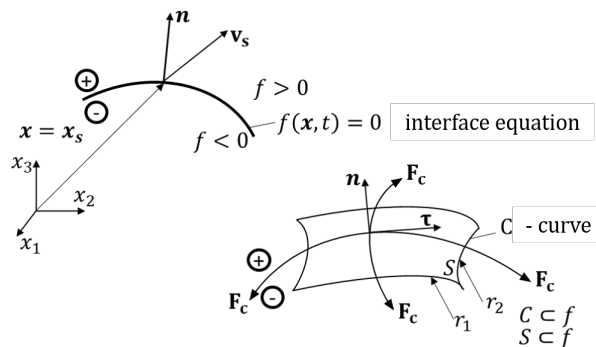


Figure 2: The interface between two immiscible fluids.

8

Stokes' formula is used to translate the capillary force from the $C$ curve to the $S$ surface.

$$\mathbf{F_c} := \oint_C \sigma \, \mathbf{n} \times d\mathbf{x} = \int_S \left(-grad\,\sigma + div\,\mathbf{n} \cdot \mathbf{n}\right) dA. \tag{3}$$

Note that the capillary force, i.e. the voltage $\sigma$, can only vary in the direction of the versor $\tau$ tangent to the surface $f$ (at the interface), implying $grad \cdot \mathbf{n} = 0$.

The following notations are used:

- $grad\,\sigma := \nabla\sigma; \, div\,\mathbf{n} := \nabla \cdot \mathbf{n}$,

- $\varphi$ is the jump in size $\varphi$ on the interface, defined as:

$$[(\varphi)] = \varphi^+ - \varphi^-, \tag{4}$$

- $H(f)$ is the Heaviside function associated with the interface, defined as:

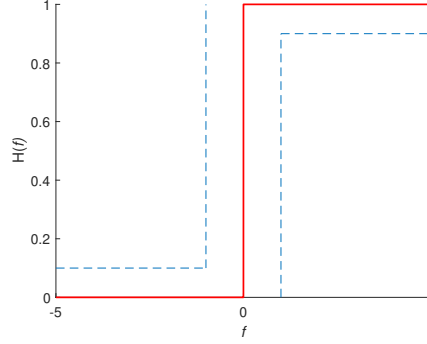$$H(f) := \begin{Bmatrix} 1, & f > 0 \\ 0, & f \leqslant 0 \end{Bmatrix}, \tag{5}$$



Figure 3: Graphical representation of the H-function.

- $\delta(f)$ is the Dirac (delta) function, defined as:

$$\frac{dH}{df} := \delta(f), \tag{6}$$

- the delta function associated with the interface is defined as:

$$\delta^s := \delta(f)\,|\nabla f|\,[1/m], \tag{7}$$

- the normal to the surface $f$ is defined as:

$$\mathbf{n} = \frac{grad\,f}{|grad\,f|} = \frac{\nabla f}{|\nabla f|}, \tag{8}$$

- surface curvature, is defined as:

$$\kappa := div\,\mathbf{n} = \nabla \cdot \mathbf{n}, \tag{9}$$

$$\kappa = \frac{1}{r_1} + \frac{1}{r_2}, \tag{10}$$

- from the Young-Laplace equation, the average surface curvature, is:

$$\kappa^* = \frac{1}{2}\left(\frac{1}{r_1} + \frac{1}{r_2}\right). \tag{11}$$

Assuming that the interface $f$ is a material surface, the condition follows that its material derivative is zero:

$$\frac{df}{dt} = 0, \tag{12}$$

$$\frac{\partial f}{\partial t} + \mathbf{v_s} \cdot grad\, f = 0, [23]. \tag{13}$$

The fluid stress integrated on the surface S is defined as:

$$\mathbf{F_s} = \int_S \mathbf{t}\, dA, \tag{14}$$

where $\mathbf{t} = \mathbf{Tn} = -p\mathbf{n} + \mathbf{T_E}\mathbf{n}$, is the stress $\mathbf{t}$ associated to the Cauchy stress tensor $\mathbf{T}$, $\mathbf{T} = \mathbf{T}^T$, $\mathbf{T} = -p\mathbf{I} + \mathbf{T_E}$, $p$ is the pressure and $\mathbf{T_E}$ is the extra-stress tensor that depends exclusively on motion/deformation (called the extra-stress tensor).

For a Newtonian fluid $\mathbf{T_E} = 2\eta_0 \mathbf{D}$, where $\eta_0\, [Pa\, s]$ is the viscosity and $\mathbf{D}$ is the specific strain rate tensor [6].

For an incompressible fluid, the trace of the specific strain rate tensor $tr\, \mathbf{D} = 0$, equivalent to $div\, \mathbf{v} = 0 = \nabla \cdot \mathbf{v} = 0$.

The equilibrium relation on the surface is:

$$[\mathbf{F_s}] = \mathbf{F_c}, \tag{15}$$

which results in:

$$\begin{cases} -[p] + \mathbf{n} \cdot [\mathbf{T_E}] \cdot \mathbf{n} = \sigma\, div\, \mathbf{n} & (normal\, eff. - Laplace) \\ \mathbf{n} \cdot [\mathbf{T_E}] \cdot (\mathbf{I} - \mathbf{n} \times \mathbf{n}) = grad_f\, \sigma & (tangential\, eff. - Marangoni) \end{cases}, [23]. \tag{16}$$

Where $\sigma = ct$ and under the assumption of adhesion of the two fluids at the interface (considered of thickness "0"):

$$\begin{matrix} [\mathbf{v}] \cdot \mathbf{n} = 0 \\ [\mathbf{v}] \times \mathbf{n} = 0 \end{matrix}, cu\, \mathbf{v}^+ = \mathbf{v}^- = \mathbf{v}_s. \tag{17}$$

It follows: $-[p] = \kappa\sigma$ with $\Delta p := p^- - p^+$ is obtained:

$$\Delta p = \sigma\left(\frac{1}{r_1} + \frac{1}{r_2}\right), \nabla_f \sigma = 0, \tag{18}$$

Laplace's formula and the jump of tangential efforts on the interface being zero.

Under these assumptions, the force acting on the interface surface reduces to:

$$\mathbf{F_c} = \int_S \sigma\kappa\mathbf{n}\, dA, \tag{19}$$

where $S \subset f$.

$\mathbf{F_c}$ acts exclusively at spatial points $\mathbf{x_s}$ where $f(\mathbf{x_s}, t) = 0$.

In the case of implementing a numerical method for calculating the dynamics of a fluid interface separating two incompressible Newtonian fluids, $f(\mathbf{x}, t) = 0$ the problem arose of introducing the force $\mathbf{F_c}$ as an additional term in the Navier-Stokes equation, obviously this acting exclusively on the interface [21, 38, 36].

The terms in the Navier-Stokes equation are specific forces per unit volume $[N/m^3]$, so $\mathbf{F_c}$ will have to be represented as a volume force [5, 45, 8], respectively:

$$\int_S \sigma\kappa\mathbf{n}\, dA = \int_{\mathfrak{D}} \sigma\kappa\mathbf{n}\delta^s\, d\mathfrak{D}, \tag{20}$$
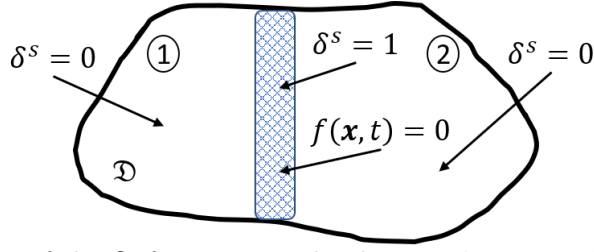
10

Figure 4: Variation of the $\delta^s$ function on the domain $\mathfrak{D}$ occupied by fluids 1 and 2.

where, $\delta^s$ is the delta function associated with the interface:

$$\delta^s = \begin{cases} 1 & \mathbf{x} = \mathbf{x_s}, \\ 0 & \mathbf{x} \neq \mathbf{x_s}, \end{cases} \tag{21}$$

defined by $f(\mathbf{x_s}, t) = 0$.

The interface is considered to separate two fluids with properties $\rho_1$, $\eta_1$ and $\rho_2$, $\eta_2$, occupying the domain $\mathfrak{D}$.

In this interpretation the local form of the Navier-Stokes equation of motion valid over the whole domain $\mathfrak{D}$, becomes:

$$\rho \left( \frac{\partial \mathbf{v}}{\partial t} + (\mathbf{v} \cdot \nabla) \mathbf{v} \right) = \rho \mathbf{b} - \nabla p + \eta \Delta \mathbf{v} + \sigma \kappa \mathbf{n} \delta^s, \tag{22}$$

where

$$\begin{aligned} \rho &= \rho_1 H(f) + \rho_2 (1 - H(f)) \\ \eta &= \eta_1 H(f) + \eta_2 (1 - H(f)) \end{aligned}. \tag{23}$$

The term in the equation (22) acting exclusively on the interface takes the form:

$$\sigma \kappa \mathbf{n} \delta^s = \sigma \kappa \nabla H(f), \tag{24}$$

where $H(f)$ is the Heaviside function associated with the interface (5) [36, 22].

## VOF Method - implementation in ANSYS Fluent

The numerical implementation of equation (22) using equation (24), involves a continuous representation of the function $H(f)$. In the case of the CSF (*Continuum Surface Force*) method, also used in the VOF (Fluid Volume) method [24, 2], $H(f) \cong \alpha$, where $\alpha$ is the volume fraction of fluid 1 in a domain consisting of two fluids separated by an interface.
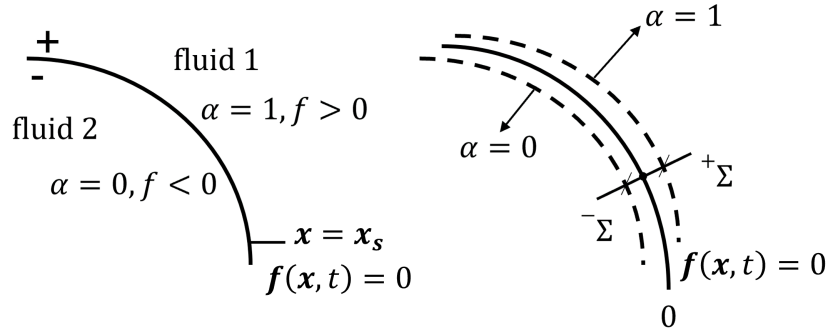


Figure 5: Representation of the volume fraction at the separation interface, where $2\Sigma$ is the thickness of the interface, theoretically $\Sigma \to 0$.

The Heaviside function on the interface $H(f)$ tracks the interface in time, so $\dfrac{dH(f)}{dt} = 0$ [23]. The volume fraction is represented by the continuous fraction $\alpha(\mathbf{x})$ which is an approximation of the function $H(f)$ in the neighborhood of the interface.
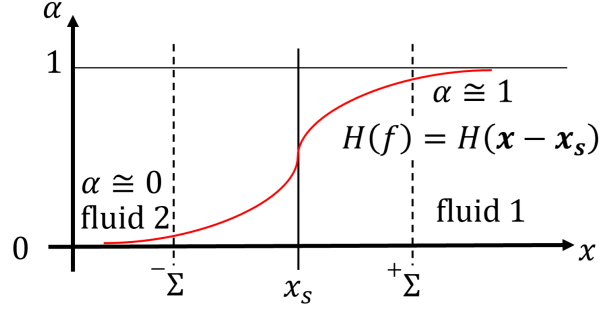
Figure 6: Volume fraction variation.

The variation of *alpha* in time is practically identical to the variation of the interface in time, so $alpha\left(\mathbf{x}, t\right)$ will have zero material derivative:

$$\frac{d\alpha}{dt} = 0; \frac{\partial \alpha}{\partial t} + \mathbf{v}\,grad\,\alpha = 0. \tag{25}$$

In Fig. 6 $\Sigma$ defines the spatial neighborhood around the interface, basically the thickness of the interface, which is directly associated in the case of the numerical solution to the spatial discretization (*mesh*) and the time step size.

Accordingly, in the VOF method implemented in the ANSYS Fluent code, for an incompressible fluid the following equations are solved:

$$\nabla \cdot \mathbf{v} = 0, \tag{26}$$

$$\rho\left(\frac{\partial \mathbf{v}}{\partial t} + \left(\mathbf{v} \cdot \nabla\right)\mathbf{v}\right) = \rho\mathbf{b} - \nabla p + \eta\Delta\mathbf{v} + \mathbf{f_c}, \tag{27}$$

with

$$\mathbf{f_c} = \beta\sigma\kappa\nabla\alpha,\, \kappa = \nabla \cdot \frac{\nabla\alpha}{|\nabla\alpha|},\, \beta = \frac{2\rho}{\rho_1 + \rho_2}, \tag{28}$$

where $\beta$ is a weight coefficient used in the ANSYS Fluent [2],

$$\frac{\partial \alpha}{\partial t} + \mathbf{v}\,grad\,\alpha = 0, \tag{29}$$

with

$$\begin{aligned} \rho &= \rho_1\alpha + \rho_2\left(1 - \alpha\right) \\ \eta &= \eta_1\alpha + \eta_2\left(1 - \alpha\right) \end{aligned}. \tag{30}$$

In the system formed by equations (26), (27) and (29) all forces are continuous forces of space and time, the unknowns being velocity $\mathbf{v}$, pressure $p$ and volume fraction $\alpha$.

**Homogeneous laminar flow**

The use of microfluidic devices allows the experimental study of various hydrodynamic phenomena. The advantage comes from the fact that small volumes of fluid are used, and the thin fluid layers homogenize the mass and heat transfer rapidly, resulting in uniform velocity, temperature and concentration distributions that will allow better control of the whole dynamic process under study.

A test laminar flow ($Re = 7.08$) is investigated in a trifurcation characteristic for microfluidics applications, Fig. 7. The characteristic microchannel dimensions are shown in Fig. 7. The channel has a 3D geometry with a depth of 50m, the discretization of the domain containing 100,000 elements. The properties of the two meshes are shown in Tab. 1.

Numerical simulations (performed in non-stationary mode up to $t = 1\ s$) are performed with two numerical codes: ANSYS Fluent and COMSOL Multiphysics. ANSYS Fluent and
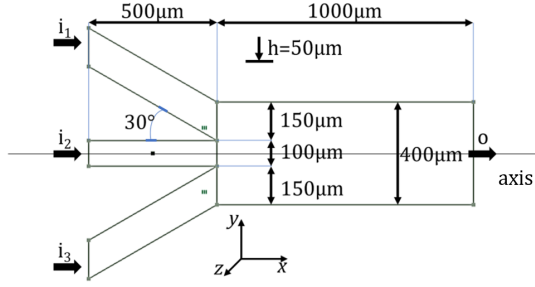
Figure 7: Microfluidic channel tested: three inputs and one output.

COMSOL Multiphysics codes are commercial numerical codes specialized in simulating fluid dynamics as well as combining fluid mechanics with electricity or magnetism. ANSYS Fluent is a code using the finite volume method, while COMSOL Multiphysics uses the finite element method.

Table 1: Mesh properties ANSYS Fluent and Comsol Multiphysics.

| Fluent | cells | faces | nodes | Min. orth. qual. | Max. A.R. |
|--------|-------|-------|-------|------------------|-----------|
| | 102635 | 318972 | 113960 | 0.86 | 10 |

| | Mesh properties | | | | |
|--------|-------|----------------|----------------|------------------|
| Comsol | elem. | Min. qual. elem. | Med. elem. qual. | Rap. vol. elem. |
| | 103942 | 0.1759 | 0.6827 | 0.002615 |

The boundary conditions imposed for this simulation are: velocity at the three inlets, zero relative pressure at the outlet and the condition of adhesion to the geometry walls. The initial condition is represented by the value of the velocity at the inlet, thus on the side inlets, $V_1 = V_3 = 0.07\,\mathrm{m/s}$ and on the central inlet $V_2 = 0.09\,\mathrm{m/s}$. The working fluid is water with the following material properties at 25°C: $\rho = 1000\,kg/m^3$ and $\eta = 1\,mPas$.

In Fig. 8, the velocity and pressure distributions on the microchannel axis are extracted from the four simulations. Good agreement is observed between the distributions obtained from ANSYS Fluent and COMSOL Multiphysics for both velocity and pressure. The average velocity resulting from both codes is $\approx 0.08$m/s, and the Reynolds number related to the main channel is $Re = 7.08$. Next, the commercial codes, ANSYS Fluent for simulating immiscible fluid dynamics and COMSOL Multiphysics for simulating dielectrophoresis in microchannels will be used.
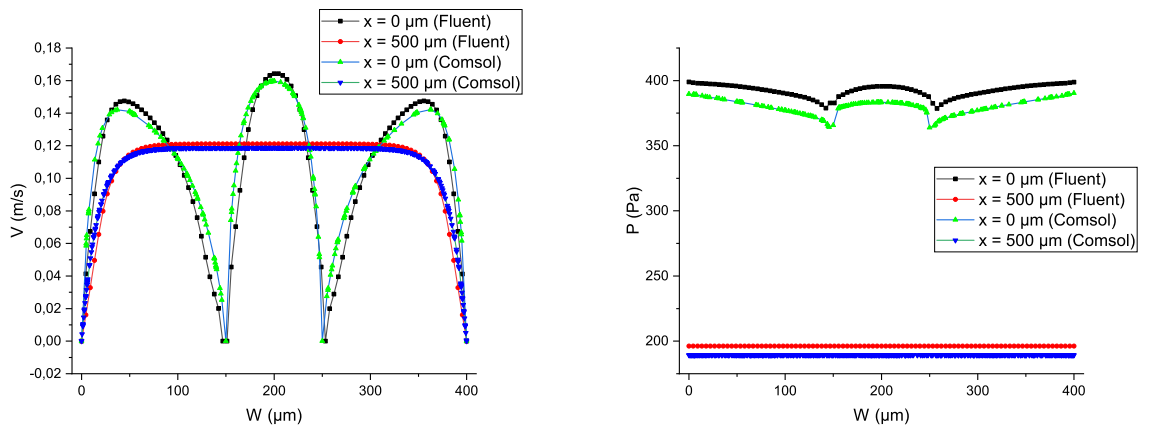


Figure 8: Velocity and pressure distributions on the midplane at junction $x = 0\mu m$ and at $x = 500\mu m$ with a Reynolds number $Re_1 = Re_3 = 5.02$ and $Re_2 = 5.97$.

**Oil-water flow in a flat channel**

The planar test case is represented by constant flow in a straight microchannel, Fig. 9.
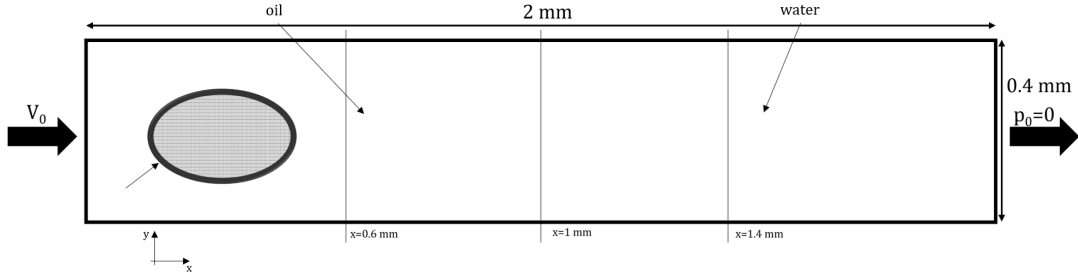
Figure 9: Discretized central microfluidic channel and representation of initial and boundary conditions.

The 2D domain is discretized, and the final network has ≈200,000 worth of elements. The boundary conditions are represented by: constant inlet velocity $V_0 = 0.01$m/s, relative pressure $p_r = 0$ at the outlet and the wall adhesion condition. The material properties of the working fluids are shown in Tab. 2, and the interfacial tension between the two fluids has the value $\sigma = 25mN/m$.

Table 2: Material properties at 25°C.

| Fluid | $\rho(kg/m^3)$ | $\eta(mPa \cdot s)$ |
|---|---|---|
| deionized water | 1000 | 1 |
| vegetable oil | 925 | 55 |

Initially the channel is filled with water (at rest) and oil is introduced at the inlet at a constant velocity $V_0$. Using this input data, the program solves the system of equations (26) - (30). For a given discretization (*mesh*) of the domain, the variations in time and space of the velocity, pressure and volume fraction $\alpha$, which defines the position and dynamics of the interface in the channel, are obtained.

The flow is laminar and non-stationary, the VOF model used is default, the interface is set as sharp (*sharp*), and the interfacial tension between the two fluids is modeled with the Continuum Surface Force method [5] see relations (26) - (30).

The residuals of the equations are set to $10^{-8}$ and the initial time step is $\Delta t = 10^{-5}\,s$. The time step adapts after each time step $\Delta t$ under the stability condition $CFL_{MAX} \leq 1$ ( the *Courant-Friedrichs-Lewy* number) and reaches the value $\Delta t = 9 \cdot 10^{-5}\,s$. The CFL number is dimensionless and is defined as the ratio of the input velocity, the time step and the smallest length of the mesh:

$$CFL = \frac{V_0\,\Delta t}{\Delta x} \leq CFL_{MAX}. \tag{31}$$

In Fig. 10 the phase contours and velocity vectors at $t = 0.1\,s$ are shown. From the representation of the velocity vectors, it can be seen that in the presence of the separation interface between the two fluids, the velocity distribution flattens out and is almost identical to that imposed at the inlet. It is thus confirmed that the interface moves at practically constant velocity (except in the area near the wall), the flow being of the type plug flow.

In Fig. 11 the interface reconstruction and velocity distributions are shown on the interface $\alpha = 0.5$, at $x = 1 \approx, mm$, in the oil phase at $x = 0.6\,mm$ and in the water phase at $x = 1.6\,mm$. It can be seen that at the interface the flow is a *plug flow*, and in the two liquid phases the velocity distribution is a parabolic one, the flow being fully developed.
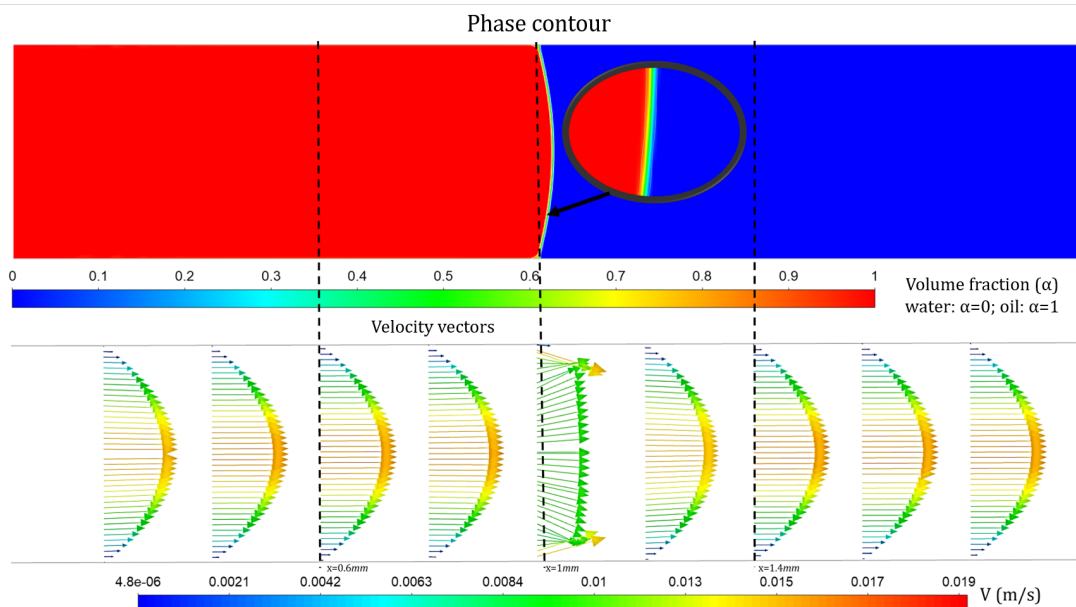
Figure 10: Phase contours and velocity vectors at $t = 0.1s$.



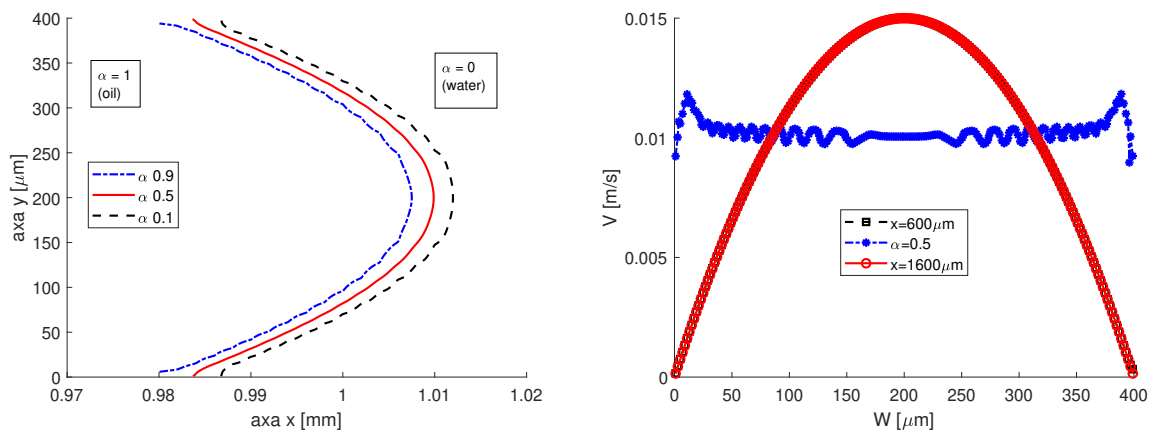Figure 11: Interface reconstruction for mesh with 200,000 elements at $t = 0.1s$. Y-axis velocity distribution before the interface at $x = 600\mu m$, on the interface $x = 1000\mu m$, $\alpha = 0.5$ and after the interface at $x = 1600\mu m$, at $t = 0.1s$.

## Multiphase flow in 3D channel with trifurcation

Multiphase flows in microchannels have applications in areas where mixing between fluid phases is required, i.e. droplet and emulsion formation [33], [9].

The microchannel in Fig. 7 was used to numerically study the formation of thin fluid films and the interface, having a dimensional ratio $h/w = 0.125$ (height over width), the motion being pseudo-planar of the Hele-Shaw type.

The shape of the interface varies with the input conditions, but is constant if the velocity ratio between the central branch and the side branches of the microchannel is kept constant. In addition, the shape of the interface also depends on the types of fluids used and the geometry. The contour of the volume fraction is shown in Fig. 12 for four numerical cases, where the velocity ratio is increased from one simulation to the other.
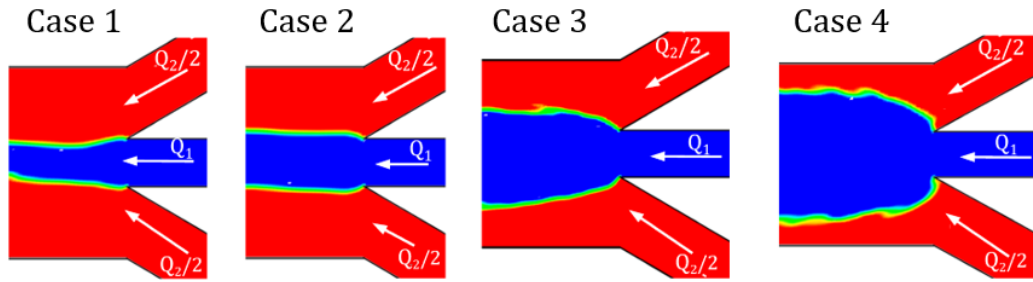
Figure 12: Volume fraction contour between the two immiscible fluids for the following velocity ratios: Case 1: $V_1/V_2 = 0.06$, Case 2: $V_1/V_2 = 0.12$, Case 3: $V_1/V_2 = 0.24$, Case 4: $V_1/V_2 = 0.8$, ©2019 IEEE [14].

## Dimensionless numbers

The dimensionless numbers used in microfluidics and analyzed throughout this thesis are shown in Table 3.

Table 3: Characteristic dimensionless numbers.

| Name | Symbol | Mathematical expression | Force ratio |
|---|---|---|---|
| Reynolds | Re | $Re = \frac{\rho V l}{\eta}$ | inertia / viscosity |
| Weber | We | $We = \frac{\rho V^2 l}{\sigma}$ | inertia / interfacial tension |
| Capillarity | Ca | $Ca = \frac{\eta V}{\sigma}$ | viscosity / interfacial tension |
| Bond | Bo | $Bo = \frac{\Delta \rho g l^2}{\sigma}$ | gravity / capillarity |
| Ohnesorge | Oh | $Oh = \frac{\eta}{\sqrt{\rho \sigma l}}$ | viscosity / inertia and interfacial tension |

# Experimental methods

## Microfluidic device manufacturing technology

In the process of making a microchannel, the first step is to choose the substrate (the material in which the microchannel is made). The type of material used for the substrate can vary depending on the desired application and is shown in Fig. 13:

- glass and polymers,

- metal,

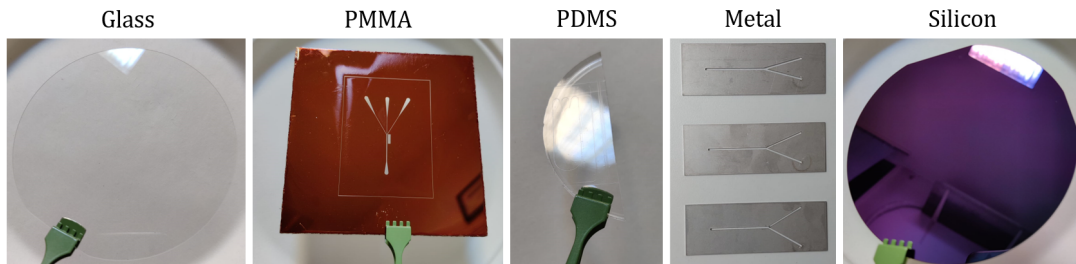- semiconductors, ceramics and composites.



Figure 13: Microchannel substrate material.

As far as polymeric materials are concerned, they offer two important advantages for the fabrication of microfluidic devices: (i) optical access and (ii) flexibility in the design of the desired geometry. Also, compared to microfluidic devices produced in silicon, the manufacturing cost is significantly reduced. Two polymers have been intensively studied and researched in

recent years for microchannel processing: PMMA (polymethylmethacrylate) and PDMS (poly-dimethylsiloxane).

The methods of manufacturing microchannels using mechanical and chemical technologies are:

- micromechanical cutting;

- dry and wet etching;

- photolithography;

- hot embossing;

- injection molding.

The methods of manufacturing microchannels using laser technologies are:

- UV laser processing;

- IR laser processing.

**Technological flow of manufacturing a trifurcation microchannel**

The microfluidic device used in the present studies is created using photolithography on a 4-inch silicon wafer. A photolithography process uses a photomask, which contains the microchannel design. A photomask is a 5-inch glass substrate over which a chromium layer is deposited. The glass-chromium substrate is coated with a positive photoresist layer. The photo-mask is obtained by direct exposure of the microchannel design using 412 nanometer wavelength radiation followed by chemical processes of development, corrosion and removal. Thus the microchannel design is obtained on the photo-mask in the desired polarity to match the subsequent processes involving the transposition of the microchannel into a PDMS matrix. The components used in the microfabrication process are shown in Fig. 14.
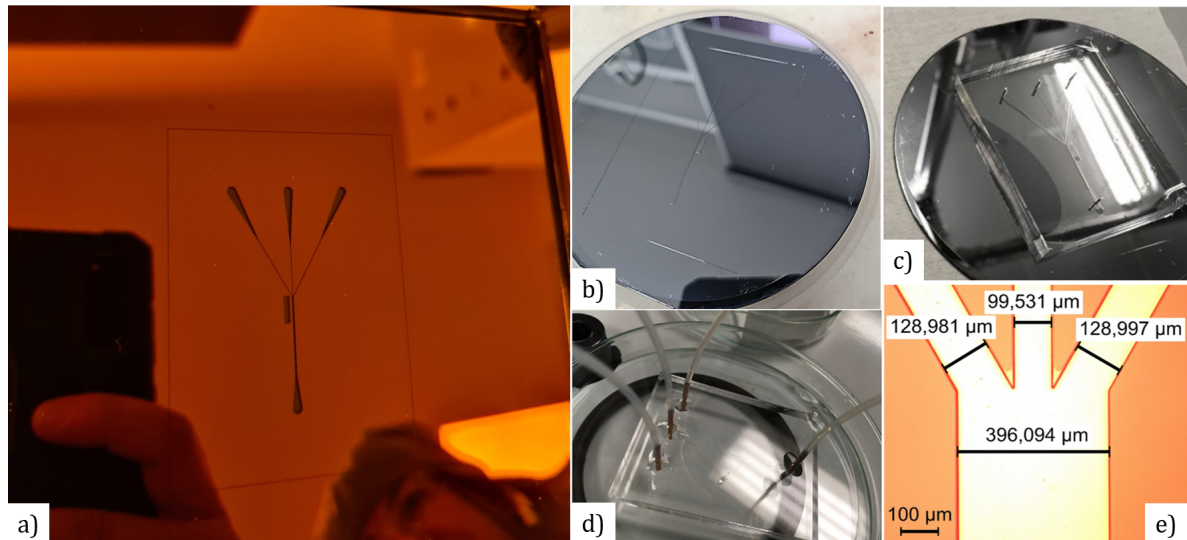


Figure 14: a) Photolithography mask, b) Silicon die, c) PDMS on silicon die, d) Microfluidic channel in PDMS sealed with glass and with ports attached, e) Detail of microchannel junction.

In the first step, a 4-inch silicon wafer is cleaned in a piranha bath (3:1 solution of sulfuric acid and hydrogen peroxide):

$$H_2SO_4 + H_2O_2, \tag{32}$$

the wafer is then washed in demonized water. These washes are followed by boiling in acetone and isopropyl alcohol. All these cleaning procedures are necessary to make the plate clean and ready for photo-etching.

After cleaning, the wafer is heat-treated in the oven at 130°C for one hour. This is followed by a plasma treatment of about 25 min which cleans the wafer of the last residues and activates its surface. This surface activation is necessary to help the photoresist adhere to the wafer surface.

The plate is etched with positive photoresist HPR504 (SU8) by centrifugation at 2500 rpm for one minute. In this way the photoresist was evenly distributed over the entire surface of the wafer. Subsequently the wafer is subjected to a heat treatment of 90°C for the photoresist to polymerize.

The microchannel mask was designed in the CleWin 5 program Fig. 14, and is now exposed on the silicon wafer. The mask is developed in caustic soda, and this ensures that the photoresist remained only in the regions outside the microchannel, as an outline. After exposure and development a heat treatment is performed at 130°C for 30 min.

The wafer is dry etched using DRIE (Deep Reactive Ion Etching). Dry etching is anisotropic and in this case is carried out at depth. In this case the photoresist layer is corroded and only the trifurcation microchannel remains on the wafer with a depth of $50 \mu m$. This depth is controlled by the pressure and flow of the gas $SF_6$. Photoresist residues are cleaned from the wafer with a plasma of $O_2$ but also with a subsequent cleaning in acetone.

In this case, the polymer used for casting is PDMS and it is prepared according to the following recipe: the base of the silicon elastomer and the curing agent are poured into a container in a volume ratio of 10:1, after which the mixture is homogenised for 5 minutes. The kit used was SYLGARD 184 (Sigma Aldrich, Chemie GmbH, Taufkirchen, Germany). The container with the mixture is left under vacuum for one hour to remove air bubbles.

During this time, the silicon wafer with the microchannel die is put to demold. This step is necessary because this demulsifier helps peel the PMDS off the die, so the surface of the silicon wafer is hydrophobicised.

The wafer is placed on a metal support and enclosed with a metal cylinder, taking care that it is as centered as possible on the wafer, and the PDMS is poured slowly into the formwork to avoid air bubbles. The assembly is placed in the oven for heat treatment at 90°C for one hour. The PDMS is stripped from the silicon wafer. The PDMS is drilled at the location of the microfluidic ports with a biomedical clamp that has an outer diameter of $1 \, mm$.

The PDMS is chemically bonded (chemical bonding) in $O_2$ plasma to a glass plate (pyrex). This glass plate will serve as a lid and thus the microchannel has been sealed. Microfluidic ports are created from 1 mm outer diameter, 1 cm long copper tubing to which microfluidic tubing (1 mm inner diameter wires) is attached. The ports are bonded to the PDMS with fast two-component epoxy adhesive. The inlet and outlet sections of the microchannel are flared in order to avoid blocking the microchannel with impurities.

Using this technology flow, shown schematically in Fig. 15, it is possible to produce a microchannel that is entirely transparent from Fig. 14 d).
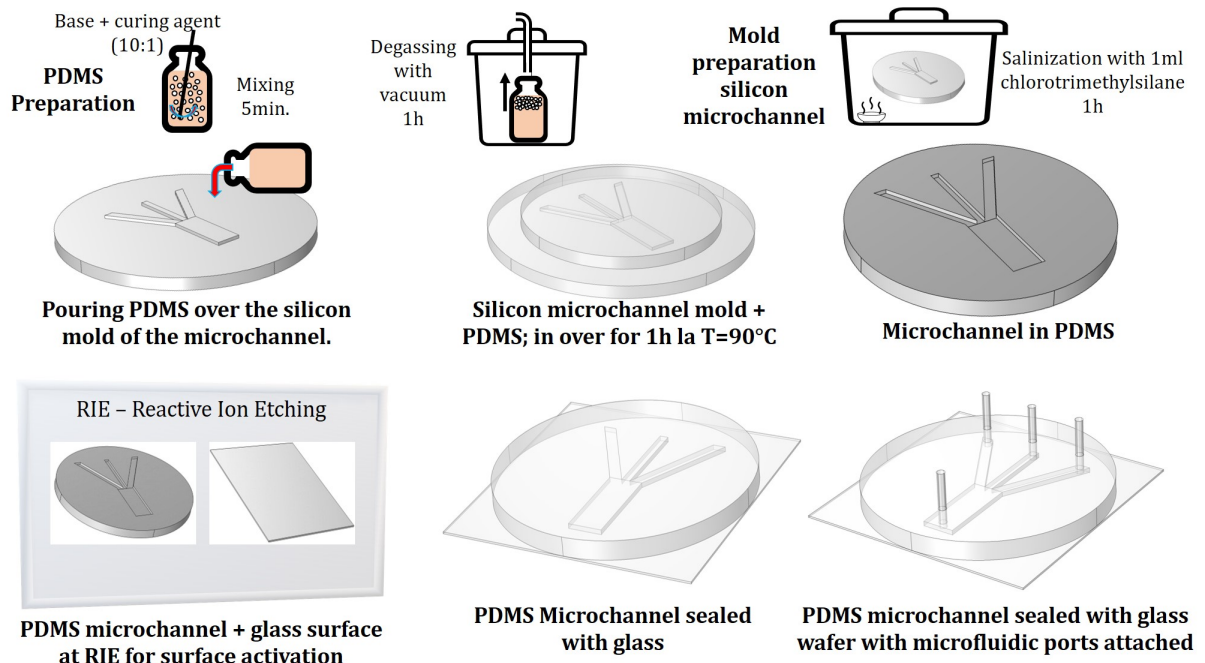
Figure 15: Technology flow for manufacturing a microfluidic device from glass and PDMS.

## Visualization and analysis techniques

Visualizing phenomena at the interface between two immiscible fluids at small spatial scales requires the use of a microscope. There are several methods for performing visualizations, but specific equipment is required for flow analysis. Thus we have:

- optical microscopy

- microPIV

The experimental setup (A) in Fig. 16 consists of a Leica inverted microscope with 10x, 20x and 40x magnification, 3 Mitos P-Pump system Dolomite Center Ltd. pressure pumps, which can be controlled by software, a light source, CCD camera (black and white), microchannel and microPIV system for velocity field determination. Both visualization and experimental measurements can be carried out with this experimental facility.
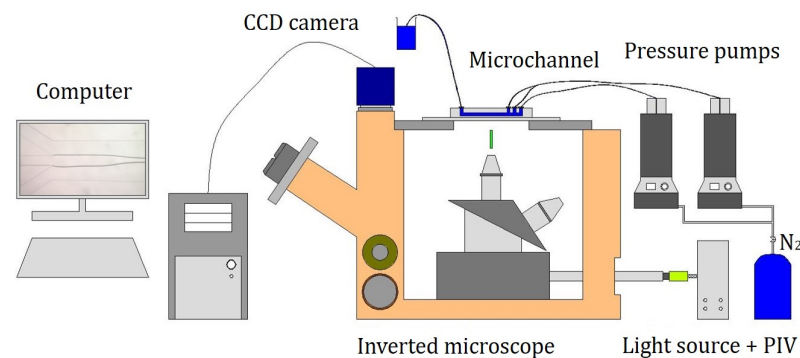


Figure 16: Sketch of the experimental setup used for visualizations and microPIV experiments (A), from NI for R&D in Microtechnologies, IMT-Bucharest, Romania.

The experimental setup (B) in Fig. 17 consists of an Olympus CKX41 inverted microscope with 10x, 20x and 30x magnification, syringe pump and CCD camera.
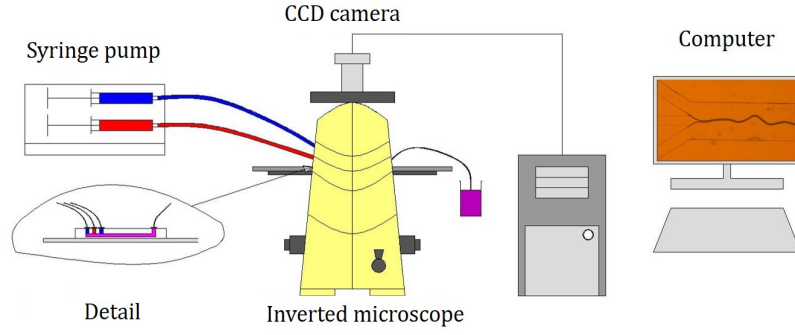
Figure 17: Sketch of the experimental set-up used for visualizations (B) from DHMHIM, University Politehnica of Bucharest, Romania.

## Optical microscopy and micro-*Particle Image Velocimetry*

Using the two experimental setups described, in Fig. 18 the following visualizations were obtained using mineral oil and isopropyl alcohol as working fluids. The correspondence of the visualizations with the input data between the two visualization systems used is performed: a) pressure controlled system (Fig. 18 a, velocities in the channel can be measured using the microPIV system); b) the controlled flow system (Fig. 18 b, velocity $V_2 = 0.086\,m/s$, $V_1 \in [0.0022, 0.022]\,m/s$), by keeping the flow/pressure constant in the side channels and increasing the flow/pressure in the central channel. Note that the flow in a side channel is $Q_2/2$.
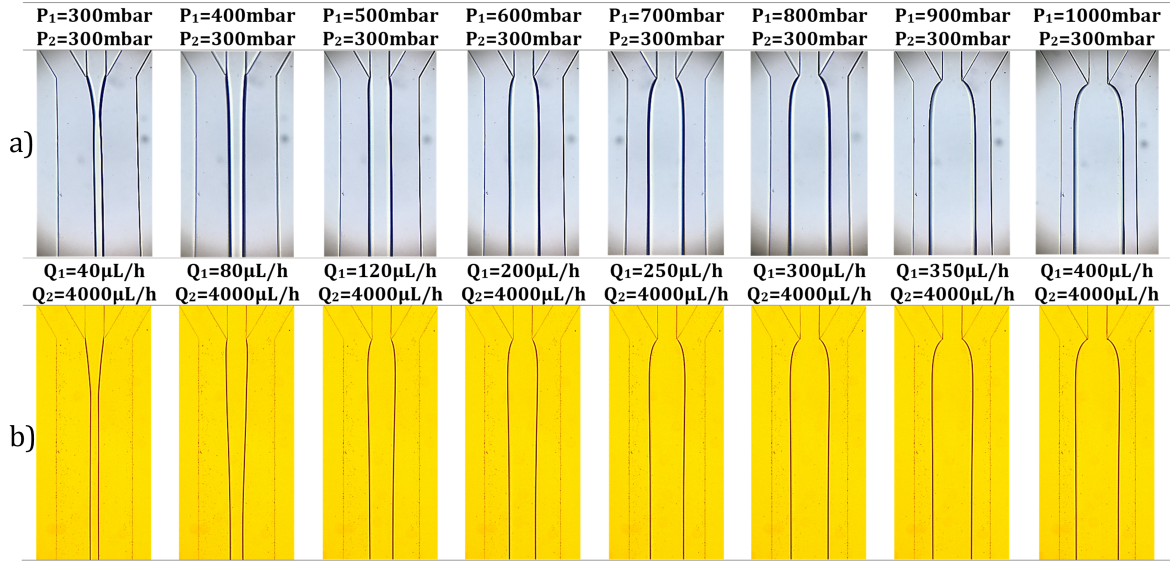


Figure 18: Visualizations of biphasic flow: a) Pressure-controlled system, in which the pressure of mineral oil in the central channel ($P_1$) is increased from $300\,mbar$ to $1000\,mbar$ and the pressure of isopropyl alcohol in the side channels is constant $P_2 = 300\,mbar$; b) Flow control system, where on the central channel the flow of mineral oil ($Q_1$) is increased from $40\mu L/h$ to $400\mu L/h$ and on the side channels the flow of isopropyl alcohol ($Q_2$) is constant $Q_2 = 4000\mu L/h$.

Experiments were performed on the trifurcation channel using red dye water on the side channels and blue dye water on the central channel. The following flow rates were imposed in the inlet experiment: $Q_1 = 2000\,\mu L/h$, corresponding to the velocity in the simulation $V_2 = 0.09\,m/s$ and $Q_2 = 4000\,\mu L/h$, corresponding to the velocities $V_1 = V_3 = 0.07\,m/s$. Thus, the flow spectrum corresponding to the numerical simulations in Fig. 8 was obtained experimentally in Fig. 19.

In Fig. 20, the presented numerical simulation is quantitatively validated with the velocity distribution obtained with the microPIV system. It can be seen that in the case of laminar flow, the velocity distribution is logarithmic, a distribution that is determined by the small size ratio
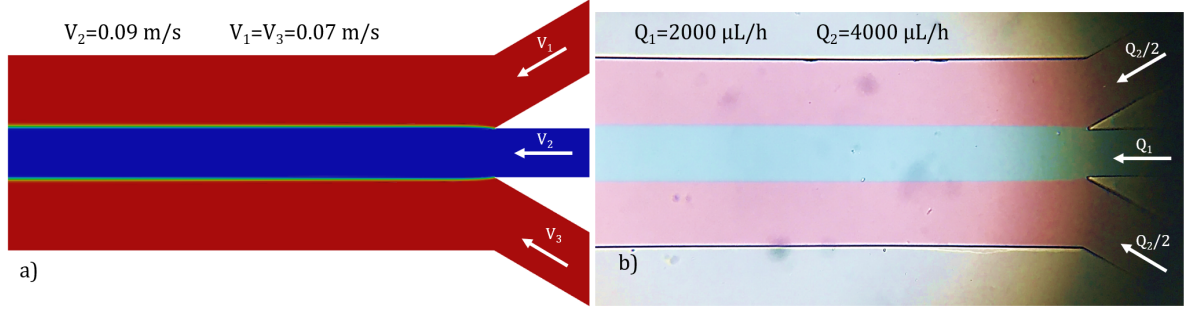
Figure 19: a) Numerical simulation of flow using VOF method in ANSYS Fluent; b) Visualization of laminar flow in trifurcation channel (see Fig. 8).

of the microchannel. Differences between the two velocity distributions occur near the wall, where the recorded particles are not on the median plane. They are experimentally generated, as can be seen from the magnitude of the measurement uncertainties.
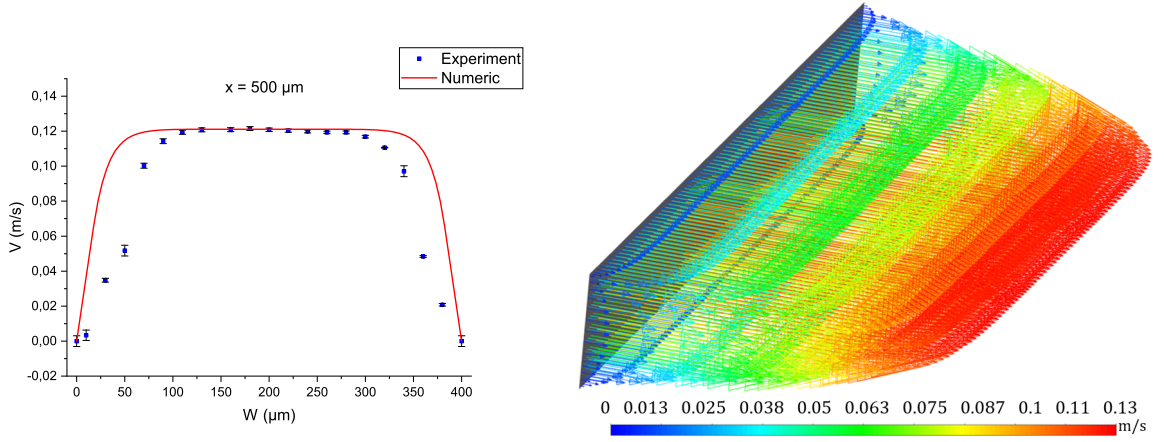


Figure 20: Quantitative validation of the numerical simulation with the velocity distribution on the median plane obtained with the microPIV system at a distance of $500\,\mu m$ from the junction and the velocity vectors from the numerical simulation.

The multiphase flow shown above in the trifurcation channel is qualitatively validated by direct experimental visualizations of the flow at the velocity ratios imposed in the simulation, Fig. 21. It can be seen that the numerical results obtained for the interface evolution in Fig. 12 are correlated with the experimental visualizations in Fig. 21. The velocities used in the experiment are shown in Tab. 4.

Table 4: Converting flow rates to velocities.

|  | Q | Q $[\mu L/h]$ | Q$[m^3/s]$ | V$[m/s]$ | $V_1/V_2$ |
|---|---|---|---|---|---|
| $Q_1$ | Case 1 | 116.28 | $3.23\cdot10^{-11}$ | 0.006 | 0.06 |
|  | Case 2 | 232.56 | $6.46e\cdot10^{-11}$ | 0.013 | 0.12 |
|  | Case 3 | 465.12 | $1.292\cdot10^{-10}$ | 0.026 | 0.24 |
|  | Case 4 | 1550.4 | $4.3\cdot10^{-10}$ | 0.086 | 0.8 |
| $Q_2/2$ |  | 2500 | $6.94\cdot10^{-10}$ | 0.108 | - |

For a quantitative validation the velocities of the numerical case with velocity ratio $V_1/V_2 = 0.06$ and an experimental case $P_1 = 400\,mbar$, $P_2 = 600\,mbar$ on a normal to flow line in the main channel ($W = 400\,\mu m$) in Fig. 22. On the vertical axis, the velocity is normalized to the maximum velocity obtained from the experiment, i.e. simulation. A good agreement of the experimental results with the numerical solution is observed.
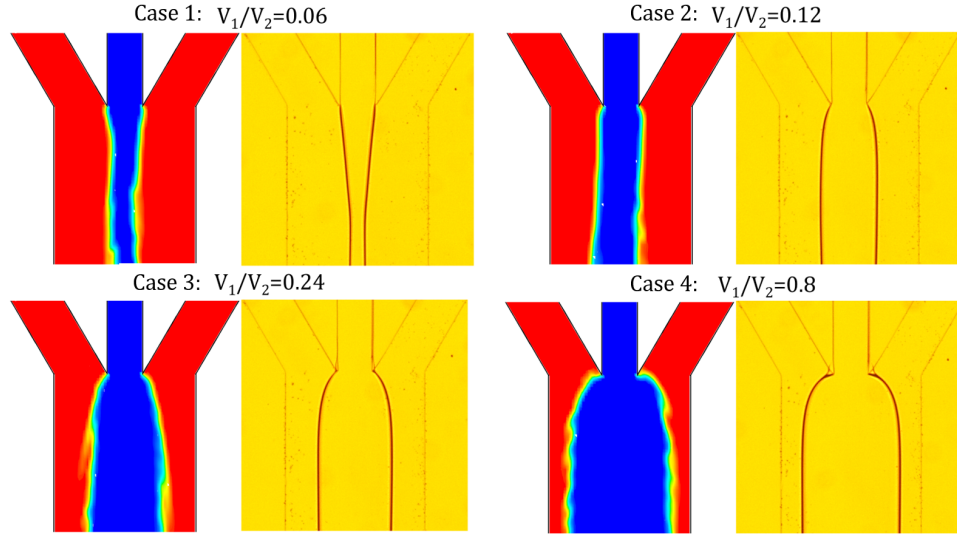
Figure 21: Numerical results after time $1\,s$ vs. experimental visualizations for different values of velocity/flow ratio at the fluid inlet to the trifurcation microchannels. It is important to note that the numerical interface is not stabilized after $1\,s$ (physical time was limited because the size of the computational time required for solution convergence is very large, on the order of days for one case).
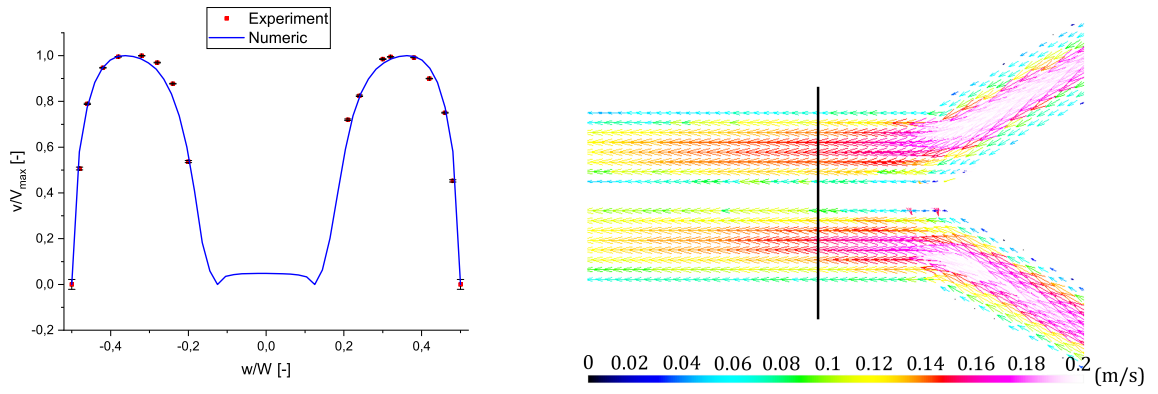


Figure 22: Comparison of the velocity distribution in dimensionless form on a line in the central microchannel between the numerical case with velocity ratio $V_1/V_2 = 0.06$ and an experimental case with $P_1 = 400\,mbar$, $P_2 = 600\,mbar$.

## Characterization of used fluids

A range of Newtonian liquids are used in experimental studies:

- deionized water

- isopropyl alcohol (IPA)

- ethyl alcohol (ETA)

- vegetable oil

- mineral oil

- glycerine water solutions

The material properties, density and viscosity, were determined experimentally. Density was determined with the mass per volume method and viscosity was determined with a rotational

rheometer in a standard oscillation test. Thus, the properties of the fluids are shown in Table Tab. 5:

Table 5: Material properties at 25°C.

| Fluid | Density [kg/m$^3$] | Viscosity [mPas] |
|---|---|---|
| deionized water | 1000 | 1 |
| isopropyl alcohol | 786 | 2.4 |
| ethyl alcohol | 789 | 1.8 |
| vegetable oil | 925 | 55 |
| mineral oil | 873 | 160 |
| Solution AG 1<br>water 21.86%<br>glycerine 78.14% | 1209.9 | 55 |
| Solution AG 2<br>water 12.5%<br>glycerine 87.5% | 1231.3 | 160 |

The interfacial tension between the various pairs of fluids used was determined with the Pendant Drop Method [16], and its values are shown in Tab. 6.

Table 6: Interfacial tension.

| Fluids | Interfacial tension [mN/m] |
|---|---|
| deionized water<br>vegetable oil | 25 |
| isopropyl alcohol<br>mineral oil | 1.2 |
| ethyl alcohol<br>mineral oil | 4.6 |
| vegetable oil<br>AG Solution 1 | 25.82 |
| mineral oil<br>AG Solution 2 | 28.46 |

# Applications

This chapter is devoted to experimental and numerical studies of the interface in microfluidic configurations commonly used in applications. The analyses are mainly performed in the geometry presented above, namely the trifurcation in Fig. 7 (or with close dimensions).

## Numerical analysis of laminar flow in a 2D geometry

In the current study the planar version of the trifurcation geometry is used, see Fig. 7, characterized by an angle between the central and lateral channels of 30°. For this case study, the aim is to correlate the results obtained with two numerical codes OpenFOAM and ANSYS Fluent, when the mass flow rate has the same value for all three inputs.

The choice of 2D geometry is justified not only because of the reduced computation time, but also because these microchannels have a very small dimensional ratio ($h/w \ll 1$) which justifies the approximation of plane motion.

In OpenFOAM, the domain is discretized using blockMesh and the mesh is characterized only by hexahedral elements with a dimension ratio of 2.5. In ANSYS Fluent, the Gambit pre-

processor was used to discretize the domain and in Tab. 7 the properties of the two *meshes* are presented.

Table 7: Mesh properties, [17] ©2019 IEEE.

| Mesh | Nodes | Cells | Faces |
|---|---|---|---|
| blockMesh | 499354 | 234200 | 959276 |
| Gambit | 161882 | 157031 | 318912 |

Since the working fluid is Newtonian, the following assumptions are valid: the fluid is incompressible, the motion is stationary and the flow regime is laminar. As such, the system of Navier-Stokes equations (1) governs the flow and is discretized using the Finite Volume Method [25] over the domain together with the continuity equation (2). As for boundary conditions, the inlet is set as the velocity at the inlet, at the outlet the relative pressure is zero and for the walls the wall adhesion condition.

Three mass flow rates have been studied and the corresponding Reynolds number is: 0.1, 0.75 and 1, calculated with the formula in Tab.3. The working fluid is water and its properties are: density $\rho = 998.2 \, kg/m^3$ and dynamic viscosity $\eta_0 = 1.003 \, mPas$. Since the inlets in the microchannel have different sizes, to have the same flow rate, the required initial velocities are: $v_A = v_C = 0.005 \, m/s$ and $v_B = 0.0075 \, m/s$. The corresponding mass flow rate is equal for all three secondary microchannels: $Q_A = Q_B = Q_C = 0.00074863 \, kg/s$.

The first parameter investigated is the velocity size and, as can be seen from Fig. 23, after the intersection of the three side channels, the velocity profile tends rapidly towards a parabolic distribution as expected when the flow regime is laminar. For this reason the results are presented only on four lines, because in the main channel after $100 \, \mu m$ the velocity distribution tends towards a parabolic profile. When comparing the two numerical codes the results are in very good agreement and the only difference between the values is in the wall approximation, because from OpenFOAM, when extracting the data, the velocity is interpolated at the cell midpoints, as such, there are no values at the mesh points to be returned.
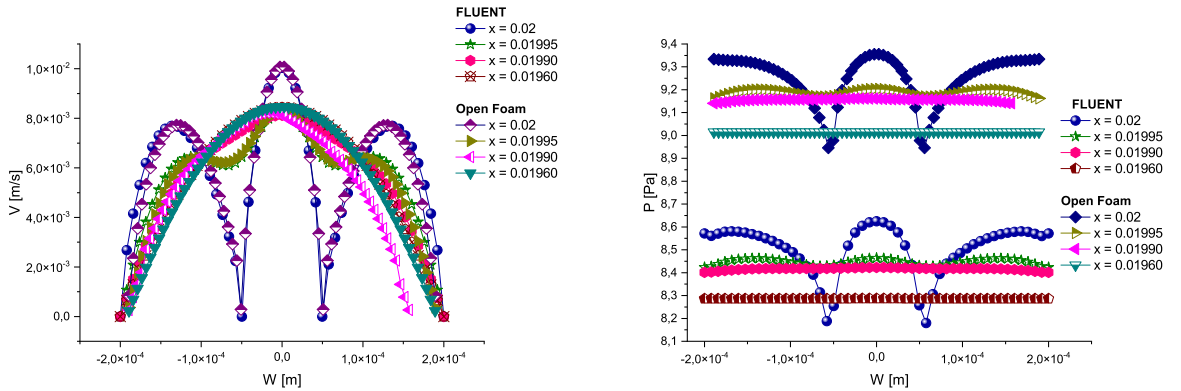


Figure 23: Comparison of velocity distribution between ANSYS Fluent and OpenFOAM on four horizontal lines after the junction. Comparison of pressure distribution on four horizontal lines after junction, [17] ©2019 IEEE.

The main difference between the two numerical codes occurs when pressure is analyzed. As can be seen from Fig. 23, even if the pressure distribution on the horizontal lines follows the same pattern, there is a difference in their values. There are several reasons for this pressure mismatch, such as the two types of algorithms that perform pressure-velocity coupling, but the only way to ensure the correctness of one code or the other is through experimental validation.

The flow was analyzed on an axis along the microchannel in Fig. 24. The velocity along the microchannel axis is characterized by two inflection points and shows a rapid decrease followed

by a small increase in its magnitude after the intersection of the three secondary microchannels. This, in turn, is explained by the fact that three equal flows enter the main microchannel, which has a larger cross-section, at the same time. Furthermore, the pressure varies along the entire axis of the microchannel and can be divided into two linear functions, but with different slopes. As can be seen, the frictional stress at the wall shows a maximum at the entrance to the main microchannel and then decreases asymptotically to the specific value of WSS at the wall of $0.06 Pa$.
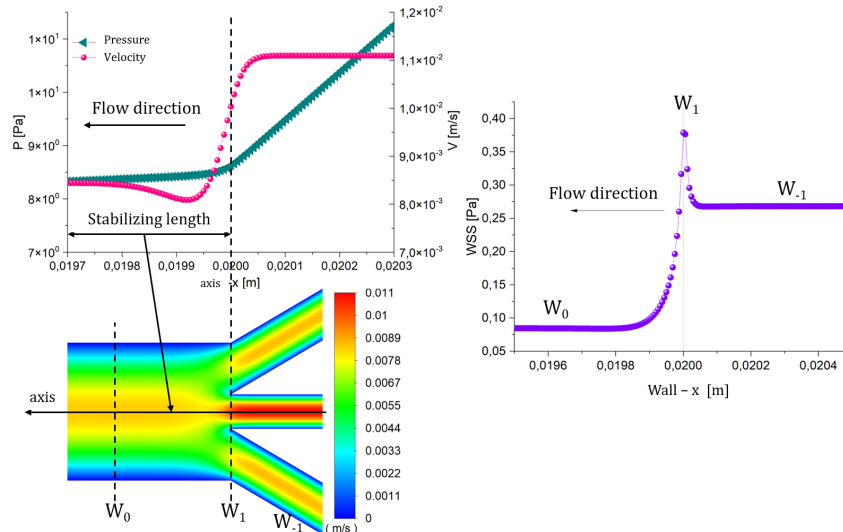
Figure 24: Pressure and velocity magnitude variations along a vertical axis in Fluent, Velocity magnitude contours - Fluent. Variation of wall shear stress on the straight wall in Fluent with location of points, [17] ©2019 IEEE.

**Influence of nanostructures on laminar flow**

Carbon nanomaterials have attracted the attention of the scientific community due to their remarkable mechanical, optical and electrical properties. Monostructured graphene-a single layer of carbon atoms arranged in a hexagonal structure, is probably the most promising carbon material due to its extraordinary properties including high transparency, good electrical conductivity, electron mobility and flexibility. When carbon nanomaterials are integrated into microfluidics, multiple advantages arise. These advantages come in the form of sensors: field-effect transistors with graphene-drained source channel [48], optical sensors [49] and biosensor [31]. Three graphene-based microfluidic devices were created in this study.

Microchannels are created on a silicon wafer by standard photo-etching. The photoresist used is AZ4562. Corrosion is performed using DRIE (deep reactive ion etching) with a Bosch process. The microchannel depth is $70\,\mu m$ and the design is shown in Fig. 25.
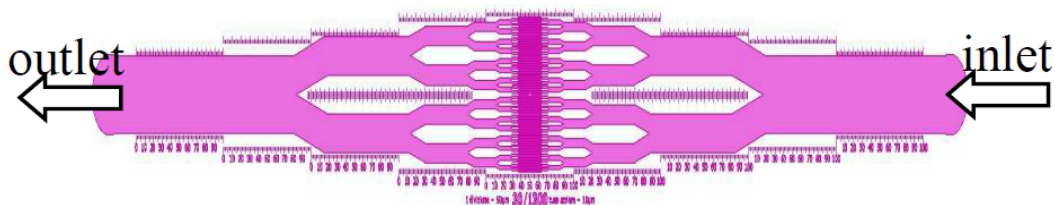
Figure 25: Microchannel design, [10] ©2021 IEEE.

Three types of carbonaceous materials are incorporated into microfluidic devices: SLG (monolayer graphene), NCG (nanocrystalline graphite) and GNW (vertical graphene); by different methods. SLG is transferred from the Cu substrate, while NCG and GNW are grown directly in the microchannel.

With microPIV the study was performed on the three microchannels using isopropyl alcohol (IPA) as working fluid. The region of interest for the microPIV study is represented by the $120\,\mu m$ branch. The influence of the bifurcation on the velocity profile is neglected, measurements are made at a distance of $240\,\mu m$ from the bifurcation. Four inlet pressures are required: 100 mbar, 200 mbar, 300 mbar and 400 mbar. The method used to correlate the velocity vectors was Average Correlation (from 100 images) with a 16x16 pixel query window. Uncertainty analysis is performed in Dantec software using the *Peak Height Ratio* method (Charonko & Vlachos, 2013).

In Fig. 26 the velocity distribution for two cases is shown. The SLG has a height of 0.3 nm and the velocity profile has a parabolic distribution in all cases. NCG has a height of 360-380 nm and its influence on the velocity profile is significant. The profile no longer has a parabolic distribution but in this case it flattens out. GNW has a height of 450 nm, and like NCG has a large influence on the velocity profile. As expected in the case of vorticity, the high values are near the walls. A uniform and consistent distribution for laminar flow is obtained for SLG in Fig. 26 B.
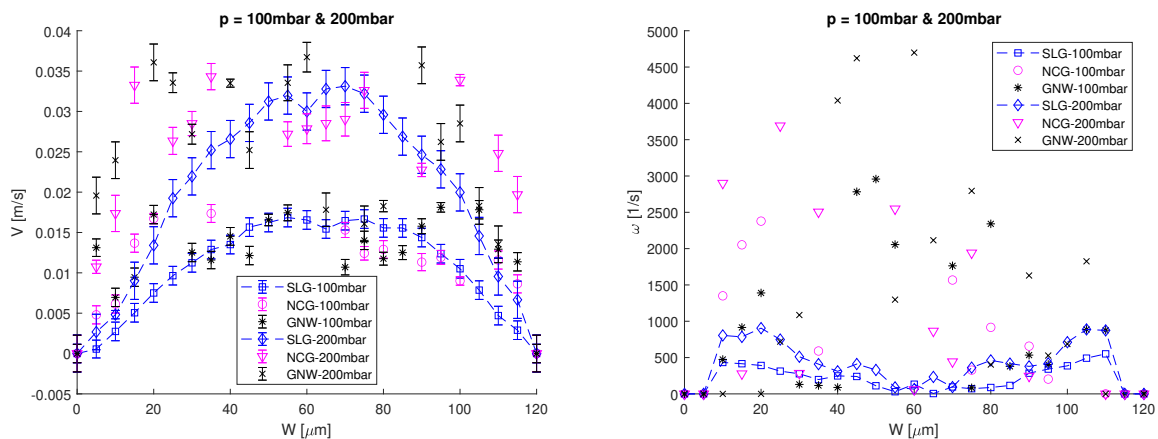


Figure 26: Distributions by. Velocity; 100 and 200 mbar inlet pressure: blue SLG (squares-100mbar, diamonds-200mbar), magenta NCG (circles-100mbar, triangles-200 mbar) and black GNW (star-100mbar, cross-200mbar); B. Vorticity; Inlet pressure of 100 and 200 mbar with the same color code, [10] ©2021 IEEE.

In the NCG and GNW cases, maximum values are recorded over the full width of the microchannel. In the SLG case, the vorticity magnitude decreases significantly in the middle of the channel, where the velocity gradient is low. This insight from the vorticity distribution highlights the influence of carbonaceous nanomaterials on the flow field.

## Multiphase flow in a Y-bifurcation microchannel

The importance of multiphase flow lies in numerous applications ranging from the human body to nature and industrial applications. Even without a phase shift, multiphase flow problems require special attention due to their complex formulation.

The evolution of the interface between deionized water and vegetable oil in a Y-bifurcation microfluidic device is investigated experimentally and numerically, Fig. 27. The experimental part consists of flow visualizations and microPIV measurements. The aim of the experimental investigations is to validate qualitatively and quantitatively the numerical simulation using the same flow conditions.

The numerical simulation performed in this study is carried out in the commercial code ANSYS Fluent. The Fluid Volume Method was used to model the evolution of the interface inside the microchannel between vegetable oil and deionized water. The domain is represented
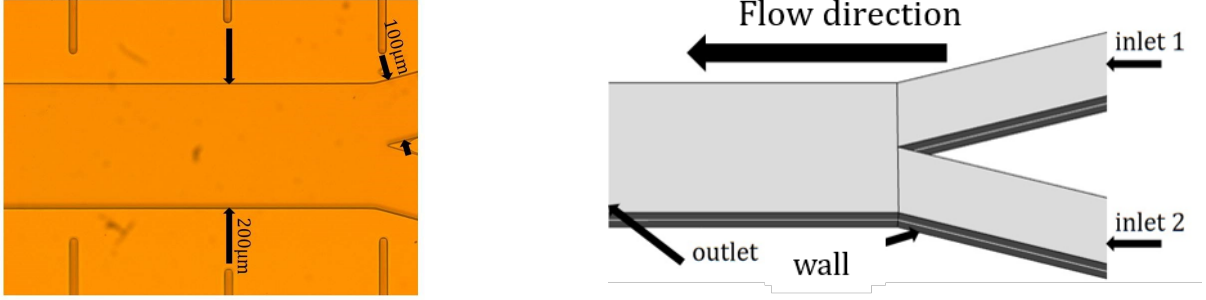
Figure 27: Characteristic dimensions of the Y-shaped PDMS microchannel, the device has a depth of h=50$\mu m$ and an angle between branches of 30°; Microchannel geometry together with boundary conditions: inlet 1 - deionized water, inlet 2 - vegetable oil, [15] ©2021 IEEE.

by the microchannel in Fig. 27. The domain is 3D and mesh of the Y-branched microchannel has 0.5 million elements, the inlet is imposed fluid velocity, at the outlet - relative pressure (equal to 0), and walls with no-slip boundary condition.

For the flow visualization part the experiment is performed using experimental setup A. The flow rates used in the experiment are imposed as initial conditions in the numerical simulation. The transition from flow to velocity is performed using the continuity equation and the results are shown in Fig. 28.
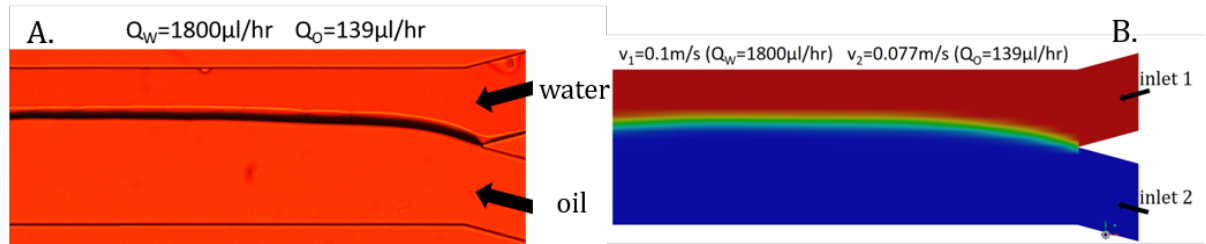


Figure 28: Qualitative validation of numerical simulation: A) Flow visualizations at specific flow rates B) Phase contours of the volume fraction (red water, blue vegetable oil)., [15] ©2021 IEEE.

In Fig. 29 data obtained from microPIV measurements are shown compared with data from numerical simulations on a straight line perpendicular to the microchannel placed 500$\mu m$ away from the Y-junction. The parabolic profile of the velocity distribution was captured within the microchannel in both the experiment and from the numerical simulation, with a slight difference of 0.02 m/s in the experiment.
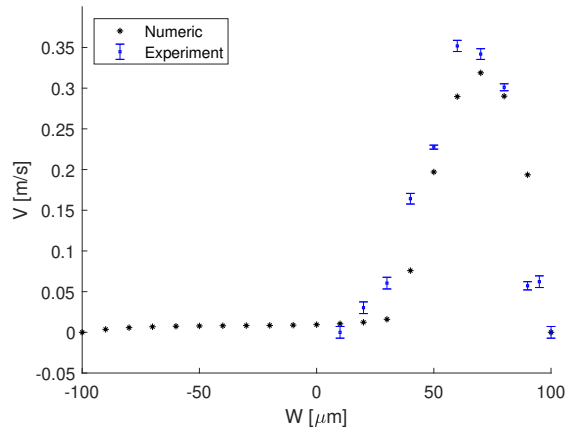


Figure 29: Quantitative validation of numerical simulation: Comparison of the velocity distribution, on a flow normal line placed 500$\mu m$ from the Y-junction, between experimental and numerical data, [15] ©2021 IEEE.

This lag may be due to the time between two pulsed lasers ($\Delta t$). For a $\Delta t = 40\mu s$, the

correlation was good, with 10 particles within a query window. Given the results in Fig. 29, $\Delta t$ should have been slightly higher.

## Multiphase flow in a microchannel with trifurcation

In multiphase flow, validation and verification of the flow field as well as the presence of multiple interfaces in the microchannel are topics of great importance in computational fluid dynamics. When fluids are immiscible, there are several methods used for interface modeling. Two main directions can be followed: surface methods and volume methods [42]. In general, in both methods, the Navier–Stokes equation is used to formulate a fluid in which a source term is added to account for surface tension effects, together with a differential equation to be solved at the interface.

In this study two 3D VOF numerical simulations are performed using two VOF formulations, namely explicit and implicit, on a reference geometry, see Fig. 7. The numerical simulations are then validated qualitatively by comparing the flow visualizations with the phase contours and validated quantitatively by comparing the velocity and vorticity distributions obtained from the simulations with the experimental data obtained from the microPIV.

The initial condition for these simulations is the input velocity value. For the side branches of the microchannel, $v_1 = v_3 = 0.1[m/s]$ and for the central branch $v_2 = 0.006[m/s]$. In addition, to shorten the simulation time, the microchannel is filled with deionized water, while the second inlet is filled with vegetable oil.

In Fig. 30, the velocity vectors are shown starting from a plane $500\,\mu m$ away from the junction. The velocity vectors are shown on a doubled scale to show the parabolic profile of the aqueous phase and its influence on the oily phase. A phenomenon was observed at the interface, due to the large difference in velocity magnitude between the two phases, the interface acts as a moving wall to which the oily phase adheres, resulting in accelerated flow near the interface for the oil phase.
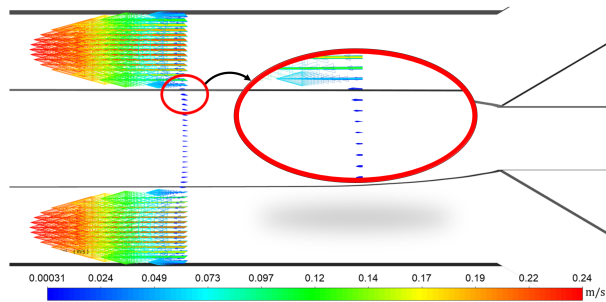


Figure 30: Increased oil phase velocity in the vicinity of the interface, [13] license CC BY 4.0.

.

The comparison between the two numerical simulations is performed, where S0 is the explicit VOF simulation performed on the 2.5M element mesh #1, while S2 is the implicit VOF simulation performed on the 1M element mesh #2. In Fig. 31, the phase contours are shown along with the spacing of the mesh for each simulation and it can be seen that the interface in S0 is more diffuse than the interface in S2, given the clear difference between the two *mesh*. Furthermore, a diffuse interface is related to the false currents generated at the [50] interface, and for explicit VOF, more false currents were generated. The mesh used for S2 has more elements after the junction than the mesh S0. In order to compare the two simulations correctly, a new numerical simulation is performed using the explicit VOF method on the mesh #1 - S1.

In Fig. 32 the velocity and vorticity distributions are shown. Shown is the evolution of the velocity distribution on the midplane from the entrance to the main channel, $x = 0\,\mu m$
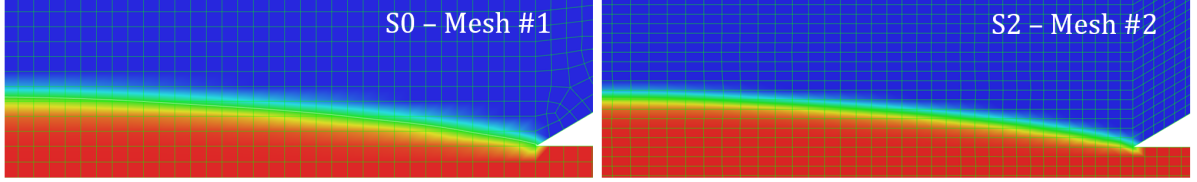
Figure 31: Details of the interface phase contours; difference between the two simulations S0 and S2 respectively. The interface thickness ($\phi$) is the difference between the volume fractions, $\alpha = 0.1$ and $\alpha = 0.9$ and for S1 $\phi_{S1} = 19.3\,\mu m$, while for S2, $\phi_{S2} = 12.8\,\mu m$, [13]

to $x = 500\,\mu m$ junction distance. At the $500\,\mu m$ boundary in the channel, the flow is fully developed and the velocity has a parabolic distribution for the aqueous phase.
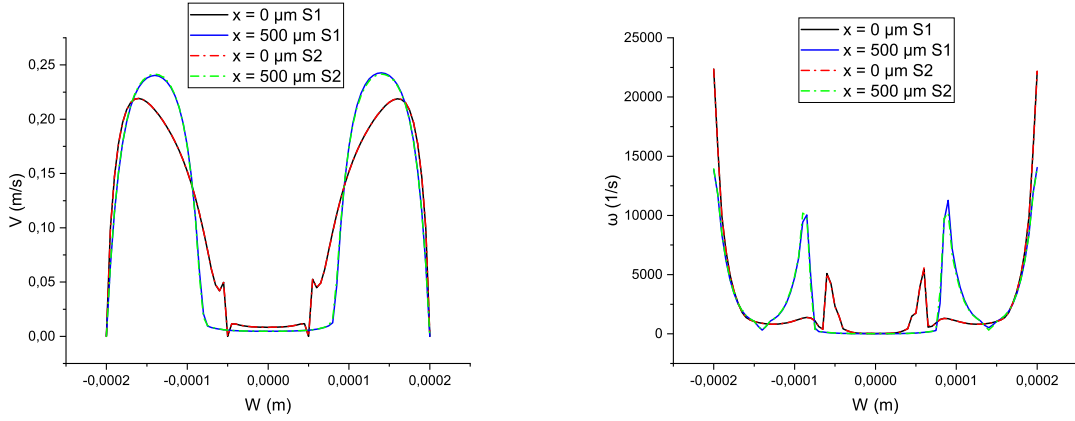


Figure 32: Distribution of velocity and vorticity on two lines inside the channel, [13] The results of the simulations S1 and S2 are almost identical.

Using the first experimental setup, the numerical simulations with flow visualizations in Fig. 33. The transition from velocity to flow is performed using the continuity equation.
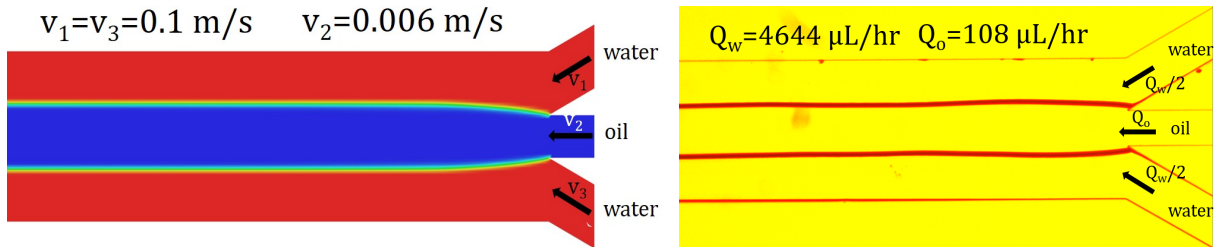


Figure 33: Experimental interfaces: qualitative validation of numerical simulation using flow visualization. The input flows in the experiments correspond to the magnitude of the mean velocities imposed in the numerical simulations, [13]

The quantitative validation of the numerical simulation is shown in Fig. 34 and is performed by comparing the velocity distribution and the z-component of the vorticity on a line perpendicular to the flow field, placed at $500\ mum$ from the junction. From the microPIV experiments, the velocity distribution obtained has a parabolic profile and matches the velocity obtained from the numerical simulation. Uncertainty analysis was performed using the particle disparity method proposed by Sciacchitano et al. [39].

The z-component of the vorticity is $\omega_z = \partial V/\partial x - \partial U/\partial y$ (where $V$ is the spanwise component and $U$ is the streamwise component of the velocity vector $\mathbf{v}$) and its distribution is shown in Fig. 34 on the right. Compared to the distribution of the vorticity magnitude, here at the interfaces we have a maximum followed by a minimum. The data points obtained from
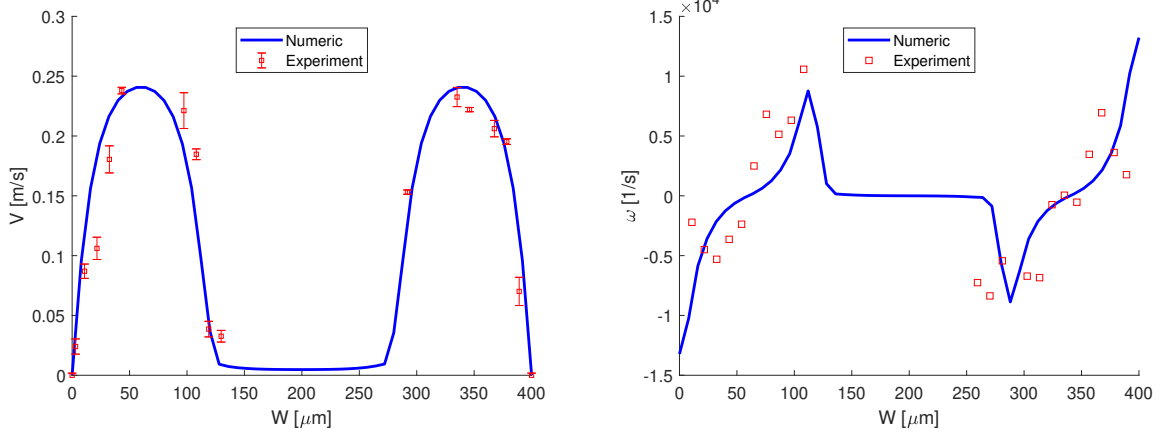
Figure 34: Quantitative validation of numerical simulation using velocity and vorticity distributions obtained from microPIV measurements, [13] license CC BY 4.0.

the experiments match the distribution obtained from the numerical simulation and also their magnitude.

## Dynamics of isoviscous fluids

The aim of this study is to investigate the evolution of the interface when we have a density contrast between the working fluids. These fluids are a vegetable oil and a mixture of water and glycerine without viscosity contrast. In this study we investigate the transition from jet to drip regime, Fig. 35.
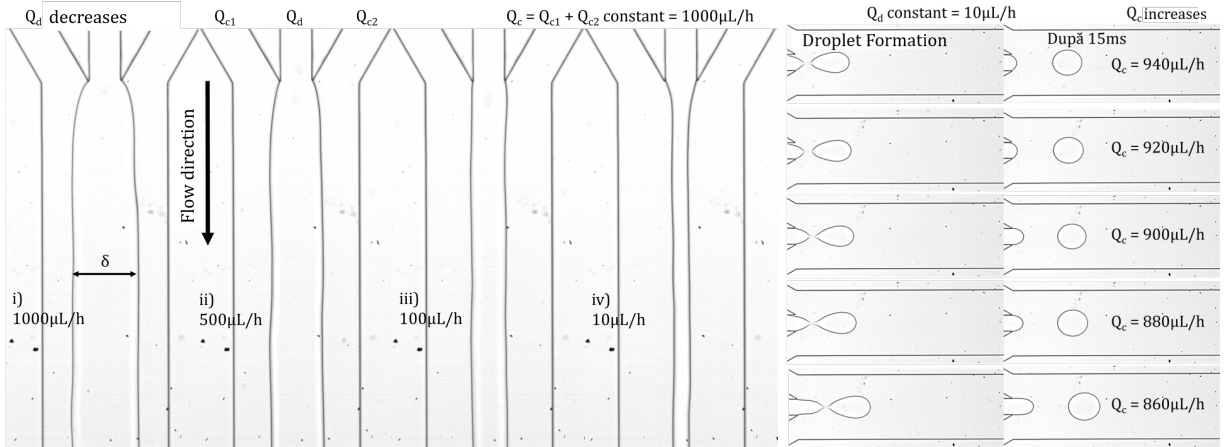


Figure 35: a) The first part of the experiment in which the dispersed phase is constant, $Q_c = 1000 \, \mu L/h$, while $Q_d$ decreases i) $1000 \mu L/h$, ii) $500 \mu L/h$, iii) $100 \mu L/h$ and iv) $10 \mu L/h$; Droplet formation within the microchannel, with dispersed phase flow rate constant at $Q_d = 10 \mu L/h$, and continuous phase flow rate decreasing from $940 \mu L/h$ to $860 \mu L/h$, [11] ©2021 IEEE.

The initial flow state is the introduction of liquids into the microchannel at flow rate $Q_c = Q_d = 1000 \mu L/h$. Since a separator is used for the side branches of the channel, the flow rate can be summed as $Q_c = Q_c1 + Q_c2$, as such on each branch, it starts at $500 \mu L/h$ at the beginning. The dispersed phase flow rate is decreased, starting at $1000 \mu L/h$ by $100 \mu L/h$ over five minutes (sufficient time for the interface to stabilize) to $100 \mu L/h$. From this point three other flow rates 50, 25 and 10 $\mu L/h$ were investigated, as can be seen in Fig.35. Dropping below this flow rate value is impossible due to the constraints imposed by the pump. The result of using this flow rate is separate flows up to the microchannel outlet ($\approx 2cm$).

The formation of droplets and their breakup from the dispersed phase is shown in Fig. 35. Five cases are shown in which the continuous phase flow rate is reduced from 940 $\mu L/h$ to 860

$\mu L/h$. On the second set of images, the droplet is shown at t=15ms after breakup. The first thing to notice is that the point in the geometry where the break occurs moves away from the junction as the continuous phase flow rate decreases.

The filament width $\delta$ was measured for each dispersed phase flow at 1 mm from the junction, and a correlation was found with the dispersed phase capillary number:

$$\delta/w = Ca_d^{0.3}. \tag{33}$$

In Fig. 36, the filament width is dimensionless with the microchannel width ($w = 388\mu m$), and the ratio $\delta/w$ as a function of the flow ratio follows the allura of the capillary number $Ca_d^{0.3}$ as a function of the flow ratio.
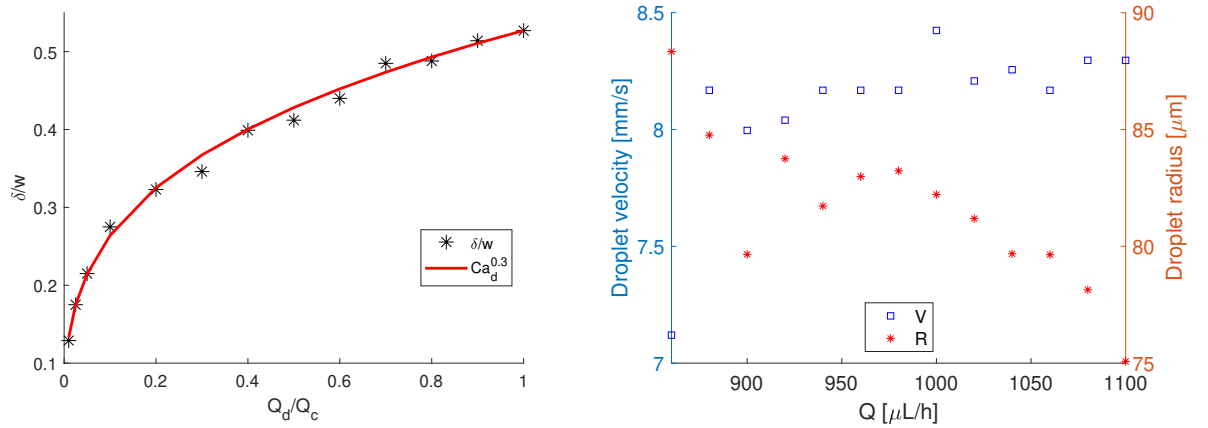


Figure 36: Correlation between filament width, $\delta$, and dispersed phase capillary number; Variation of droplet velocity and radius as a function of $Q_c$, [11] ©2021 IEEE.

The droplet velocity has a small variation around 8 mm/s for almost the whole $Q_c$ range (860 1100 $\mu L/h$), as can be seen in Fig. 36. Only at $Q_c = 860\mu L/h$ the droplet velocity decreases to $\approx$7mm/s. However, compared to the velocity of the dispersed phase (V=0.55 mm/s), the droplet velocity is actually increased by the continuous flow phase. This was measured using ImageJ for each case at the same point of the geometry between two consecutive frames. Images were acquired at 4000 frames per second. The droplet radius has an inverse variation with the flow velocity.

## Influence of gravity on the hysteresis cycle

Although hysteresis is a phenomenon specific to magnetism and electricity, it has been previously reported in fluids [40], [30], [20]. The importance of this phenomenon derives from the fact that many applications can be affected by it. For example, when testing flow regimes in a microchannel, experiments are extended over a long period of time and the microchannel is subject to hysteresis behavior. In this study, the hysteresis phenomenon in multiphase flow in a microchannel using two immiscible liquids with low interfacial tension between them, mineral oil and isopropyl alcohol, was investigated by experiments and numerical simulations. The influence of gravity on the hysteresis cycle and flow field was also evaluated.

The experimental setup consists of two microscopes, one regular and one inverted, pressure pumps and an image acquisition system, and a schematic of it is shown in Fig. 37. The PDMS microchannel can be used with both microscopes, while the silicon microchannel can only be used with the inverted microscope.
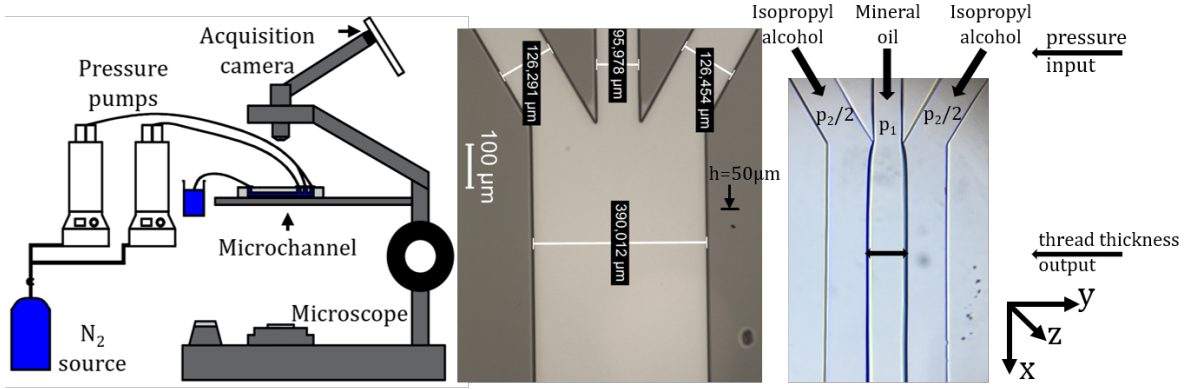
Figure 37: Microchannel design, experimental set-up scheme, PDMS microchannel characteristic dimensions and hysteresis set-up, [12].

By confining the geometry it is possible to stabilize the flow without the occurrence of instabilities [34], but in the case of a small Hele-Shaw channel, this further contributes to the stabilization of the flow [7]. This phenomenon occurs when, starting from the initial pair of pressures at the microchannel inlets, the pressure on the sides is kept constant and the pressure on the central branch of the channel is varied so that, at the same pair of pressures, a different filament width is obtained. The pressure on the central branch of the microchannel, $p_1$, is varied in four steps with a step of $20mbar$: i) from 600 to $700mbar$; ii) from 600 to $800mbar$; iii) from 600 to $900mbar$ and iv) from 600 to $1000mbar$.

In Fig. 38 and Fig. 39 the three hysteresis cycles for the four stages are compared, when the maximum pressure is 700, 800, 900 and 1000 $mbar$. In all cases the influence of gravity is observed. There is a small difference between the initial filament thickness when $p_1 = p_2 = 600mbar$. This difference is always present, especially when moving from one experiment to another.
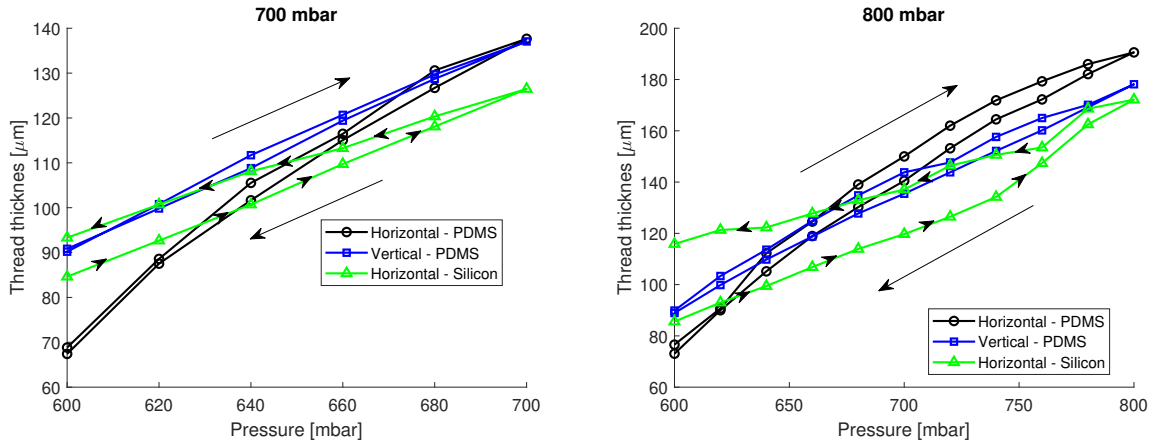


Figure 38: Hysteresis cycle stage I. 600 - $700mbar$ & II. 600 - $800mbar$, [12].

The hysteresis cycle area was investigated for all stages and is shown in Fig. 40. For the first two stages, the area obtained for the silicon microchannel is much larger than that obtained for the PDMS microchannel. Material properties play an important role in this case. PDMS is an elastic material that deforms under high pressure. In this case, it attenuates the pressure variation in the system. In opposition is silicon, which is a rigid material and transfers the pressure change directly into the microchannel. In all cases, the hysteresis surface for the horizontal microchannel is larger than that obtained for the vertical channel, so gravity reduces the hysteresis surface which represents the dissipated energy of the system.

The difference between the numerical simulations is obtained for the pressure distributions in Fig. 40. The pressure distributions are shown on six lines perpendicular to the flow field,
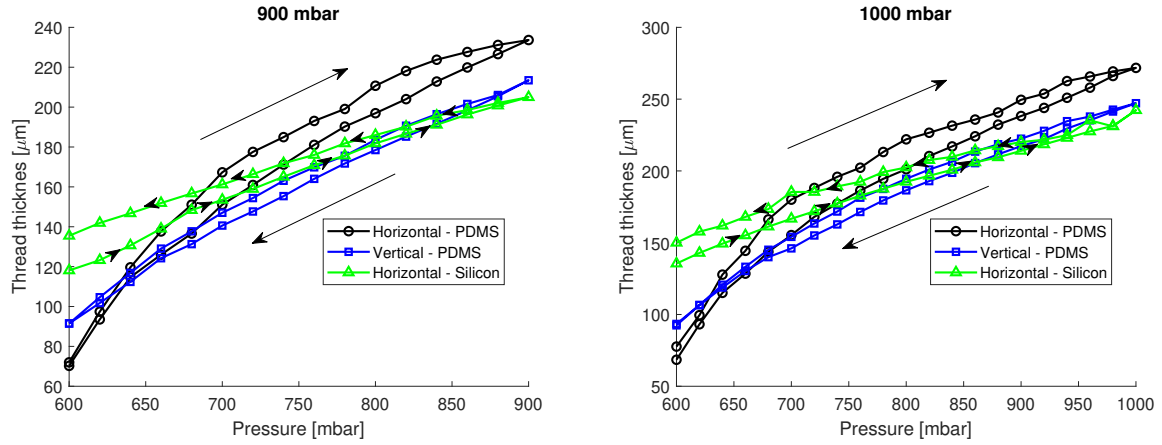
Figure 39: Stage III of the hysteresis cycle. 600 - 900$mbar$ & IV. 600 - 1000$mbar$, [12].

starting at the junction, with a step of $100\mu m$. For both pressure distributions, there are pressure jumps at the interface, which means that the interface is not straight and has a curvature. The main difference occurs in the magnitude of the pressure, which means that less pressure is required to flow in the case of the microchannel that is placed vertically, since there is a difference of $approx 40 Pa$ between the two distributions.
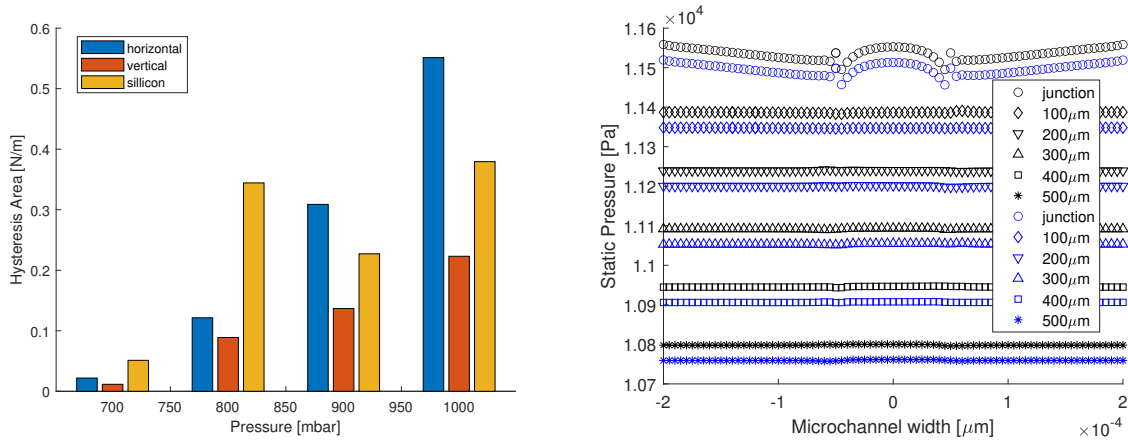


Figure 40: Comparison of hysteresis cycle area when the microchannel is microfabricated from PDMS and silicon; Pressure distributions on lines perpendicular to the flow field at $t = 1s$, black horizontal channel, blue vertical channel, [12].

## Particle/cell separation methods

The particle separation process is of major importance in the medical, chemical, biological, food and environmental fields. The predominant flow regime in microfluidic devices is the laminar regime. This allows for precise flow control and predictability.

Particle separation in microchannels can be achieved by a number of methods: passive, active and combined [37]. Passive methods are based on microchannel geometry, precise flow control and interaction between particles and geometry without being influenced by external fields. Active methods use external fields, of different types, simple geometries and generally perform better than passive methods, only in this case the complexity of the system is increased.

### Dielectrophoretic device - numeric

Dielectrophoresis is the phenomenon that controls the movement of particles due to the application of an electric field gradient, which induces a dipole moment on the cells, which is due

to the electrical polarizability of the cell membrane while moving in a suspension medium. The cell is translocated in the electric field until it reaches electrostatic equilibrium. This movement is due to the dielectrophoretic force ($\mathbf{f_{DEP}}$).

The dielectrophoretic force is described as the product of the real part of the Claussius-Mossotti factor, the radius of the cell, r, the electric permittivity of the vacuum, $\varepsilon_0$, the electric permittivity of the suspension, $\varepsilon_m$, and the squared gradient of the electric field, as follows:

$$\mathbf{f_{DEP}} = 2\pi r^3 \varepsilon_0 \varepsilon_m Re\left[CM\right] \nabla \left|\mathbf{E^2}\right| \tag{34}$$

The Claussius-Mossotti complex factor is calculated:

$$CM\left(\omega\right) = \frac{\varepsilon_p^* - \varepsilon_m^*}{\varepsilon_p^* + 2 \cdot \varepsilon_m^*} \tag{35}$$

where, $\omega$ is the angular frequency, $\varepsilon_p^*$ and $\varepsilon_m^*$ are the calculated complex permittivities of the particles and medium respectively:

$$\varepsilon_p^* = \varepsilon_p - j\frac{\sigma_p}{\omega},$$

$$\varepsilon_m^* = \varepsilon_m - j\frac{\sigma_m}{\omega}, \tag{36}$$

where $\sigma_p$ and $\sigma_m$ are the electrical conductivities of the particle or the medium.

Numerical simulations were performed in COMSOL Multiphysics [18]. These are divided into three stages: i) laminar flow (for suspension) – to determine the velocity and pressure fields; ii) electric currents (for electrodes) – to determine the electric field and iii) particle trajectories, which use the first two stages as initial solutions.

As for the boundary conditions for laminar flow, the inlet is velocity imposed and the outlets have the relative pressure imposed at zero. The walls of the geometry are set with the wall adhesion condition, Fig. 41. .
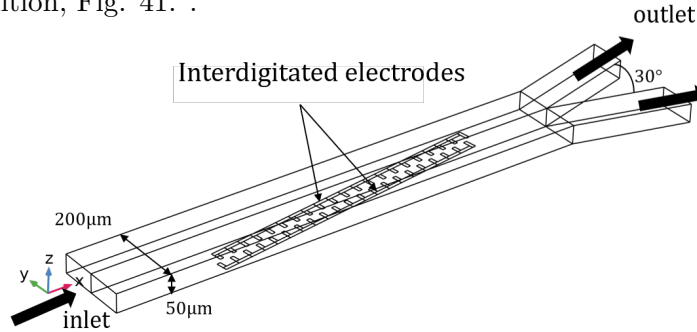


Figure 41: Dielectrophoretic device design and boundary conditions.

At the inlet the velocity $V = 100\mu m/s$ is required, at the two outlets the relative pressure is zero and for the walls the wall adhesion condition is required. The working fluid used is a mixture, specific for cell cultures, but having the same material properties as water. For the electricity part the imposed peak-to-peak electric potential is $V_{pp} = 10V$ and varies in the range $(-5 : +5V)$, and the frequency of the alternating electric field takes the following values $f_1 = 1.25 \cdot 10^5 Hz$ and $f_2 = 1.75 \cdot 10^8 Hz$. For the particle trajectory tracking part, the particle properties given in [47] are used.

In the particle trajectory calculation step, the first two modules are incorporated as initial solutions to create an environment in which particles can be released and their trajectories manipulated. It is Newton's second law that governs the trajectory of a particle:

$$m_p \frac{d\mathbf{v}}{dt} = \sum \mathbf{F_{ext}} = \mathbf{F_{DEP}} + \mathbf{F_D} \tag{37}$$

where the external forces acting on the particle are, in this case, the drag force and the dielec-trophoretic force.

In Fig. 42 are shown the results obtained after the first calculation step, where the initial imposed velocity was $100\mu m/s$. In the velocity contour, the velocity has a maximum value of $215\mu m/s$ and this is reached after the bifurcation, when the section narrows on the two branches of the bifurcation. From the pressure contour, the pressure in the whole system is low, with a maximum value of 1.15 Pa.
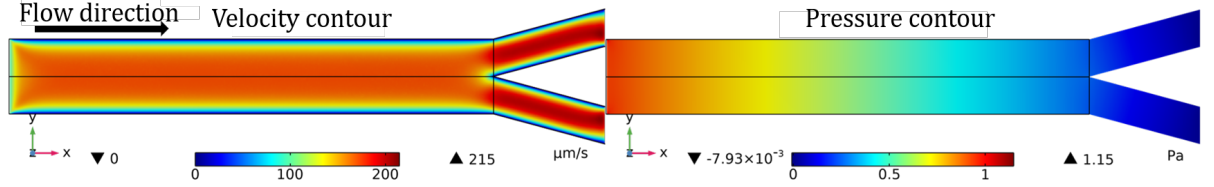


Figure 42: Velocity and pressure contours.

The results of the second stage are shown in Fig. 43 in which the electric potential variation and the electric field variation in the device are obtained. Large electric field gradients are obtained between the two interdigitated electrodes.
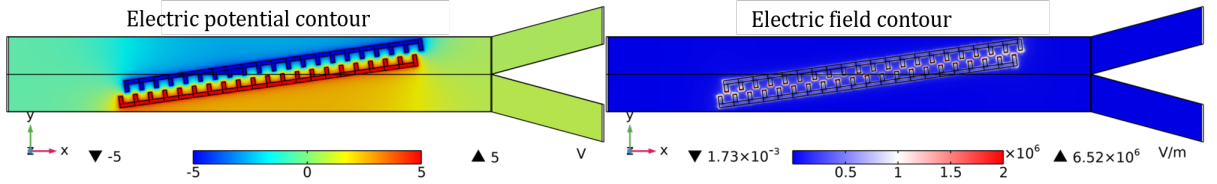


Figure 43: Variation of electric potential and electric field.

The Clausius-Mossotti factor was calculated using the classical formula. By comparing with the results from [47], the two plots have the same distribution after $10^6$Hz. The two distributions are shown in Fig. 44.
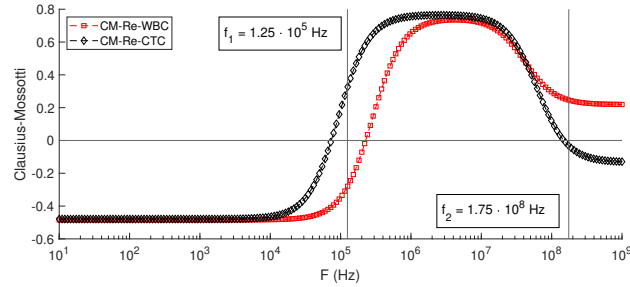


Figure 44: The real part of the Clausius-Mossotti factor for the two cell types.

The results of the last stage are shown in Fig. 45. When $f_1 = 1.25 \cdot 10^5 Hz$, circulating tumor cells are affected by positive dielectrophoresis and their trajectory is deflected towards the area with high electric field gradients. In contrast, white blood cells (WBCs) are affected by negative dielectrophoresis and their trajectory is deflected towards the area of the device where the electric field is minimal. When $f_2 = 1.75 \cdot 10^8 Hz$ the behaviour of the cells is reversed. Thus, CTCs are affected by negative dielectrophoresis and their trajectory is deflected towards the area of minimum electric field. WBCs are affected by positive dielectrophoresis and their trajectory is deflected towards areas of high electric field gradients.

Figure 45: Particle trajectories for the two simulations.

## Dielectrophoretic device - experimental

The device used in the numerical simulations was experimentally microfabricated. In the first step, gold electrodes are created on the glass wafer by depositing a 10/200 nm Cr/Au layer by electron beam deposition, and by the *lift-off* procedure the gold around the electrodes is removed. The second step consisted of creating the microfluidic channel in PDMS. The most difficult step in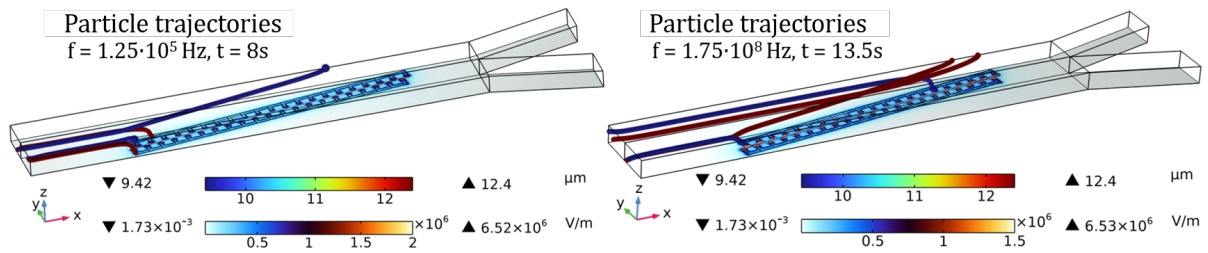 creating this dielectrophoretic device was aligning the glass electrodes to the microfluidic channel. After alignment, a textolite plate containing two pads for connecting the signal generator was glued underneath the device. The glass pad is connected to the textolite plate by two $25\,\mu m$ gold wires. Finally the microfluidic ports are attached and the final device is shown in Fig. 46.
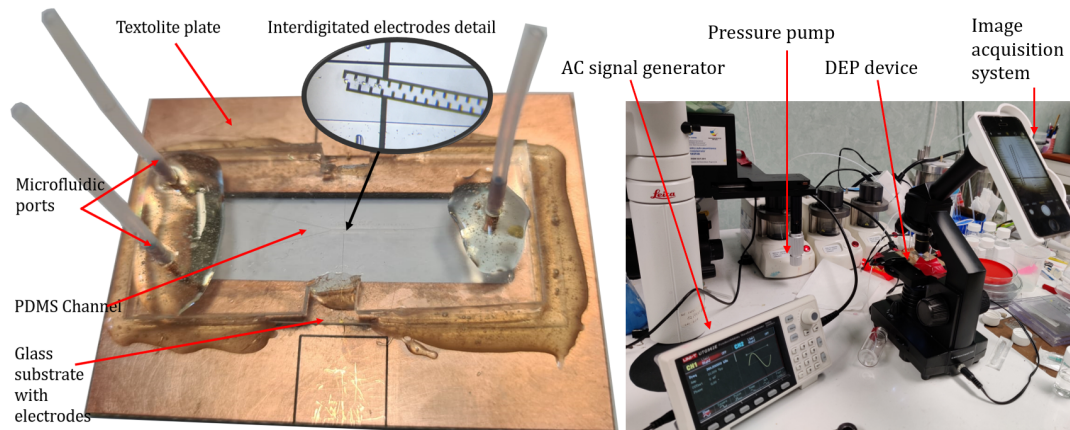

Figure 46: Experimental dielectrophoretic device.

In Fig. 47 the experimental results obtained with the dielectrophoretic device are shown. The working fluid was PBS (*phosphate buffered saline*) and three types of particles were textured: fluorescent polystyrene particles, used for microPIV studies, red blood cells and hollow glass spheres on the inside. Particles for microPIV have an outer diameter of 1m and showed no electric field response at any imposed frequency. At high frequencies, starting at 500 kHz the red blood cells were attracted to the electrodes when they reached the electrode area, thus moving to the left side of the device. If the speed of the red blood cells was very high, they passed through the alternating electric field area without being affected by it. In the last experiment, the glass spheres behaved in the same way as the particles used in the microPIV, unaffected by the presence of the alternating electric field.

microPIV Particles  After 1s  Red Blood Cells  After 1s  Hollow glass spheres  After 1s

Figure 47: Dielectrophoresis experiment with bifurcation device.

# Conclusions and perspectives

## Main contributions of the thesis

This thesis contributes to the understanding of interfacial phenomena occurring in microfluidic devices at the contact between two immiscible liquids, the factor that generates flow stability being the low dimensional aspect of the devices. In this sense, flow stability allows the investigation and modelling of the separation surface between two immiscible fluids in detail until instabilities appear.
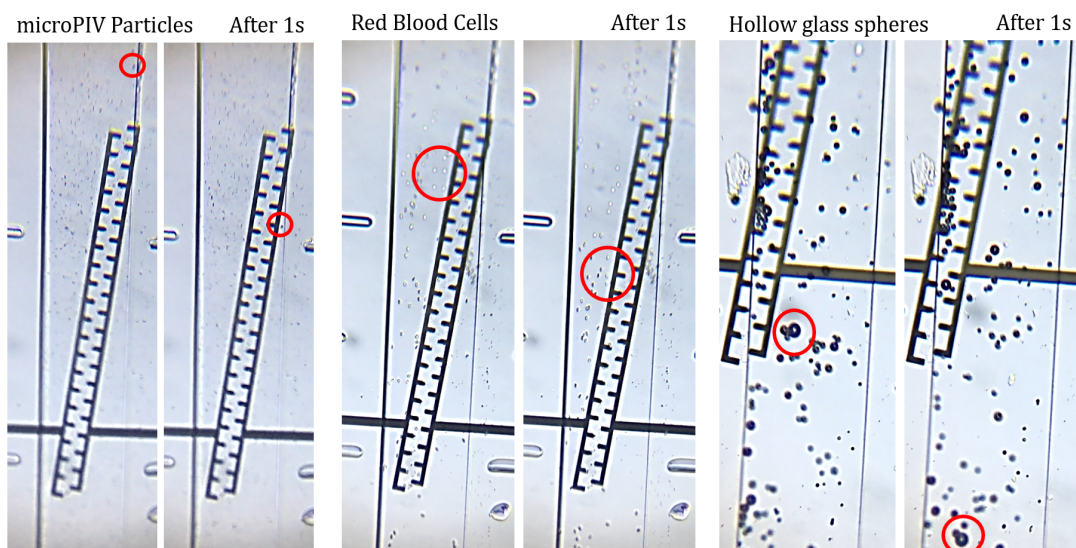
In the first part of the thesis the fundamental theoretical aspects underlying the flow of fluids in microchannels were introduced. The method of numerical calculation in the case of multiphase flow in the absence of diffusion between phases was presented.

In the second part of the thesis the methods of microchannel fabrication were presented. The technological flow used to create the microfluidic devices used in this thesis was presented. The experimental setup used to study flow dynamics through direct visualizations and velocity measurements using the microPIV technique was presented. The geometry proposed for study is a 3D trifurcation with a height to width ratio $h/w = 0.125$, with $w = 400\,\mu m$. Numerical simulations were performed using the VOF method implemented in ANSYS Fluent numerical code.

The third part of the thesis contains the developed applications based on the investigated microfluidic configurations. The applications start from the study of laminar flow, continue with investigations of flows with immiscible fluids and end with experimental and numerical investigations of the influence of the external field on the separation interface between two immiscible fluids. In the first application the flow was investigated numerically when on the three microchannel inlets the Reynolds number value was the same. The most important result of this study is the determination of the flow stabilization length in the main microchannel. In the second application the influence of nanostructures on laminar flow was investigated, thus the increased wall roughness induced strong variations of the velocity profile and increased values of the vorticity.

Two benchmark applications in microfluidics have been created through numerical and experimental investigations of multiphase flow and an answer to the central question of this thesis has been provided: "What happens at the interface?" by validating numerical simulations with experiments. Thus, from the distribution of frictional stress and pressure on the interface line it is observed that at the point where the curvature of the interface is maximum (at a distance of $25\,\mu m$ downstream of the junction) the frictional stress values are approximately four times higher than downstream (where the interface is practically flat), the pressure jump being maximum, proportional to the interfacial tension value.

In the following two applications, multiphase flow through alcohol jets in oil and isovascosic fluids was investigated experimentally. In the case of alcohol jets, the viscosity ratio, $beta$, between the continuous phase and the dispersed phase is very high ($beta \approx 80$), so that at high values of the pressure on the dispersed phase (jet) the velocity profile is accelerated near the

interface. In the case of isoviscous fluids ($beta \approx 1$), in the jet regime the jet width has been correlated with the capillary number of the dispersed phase, and in the drip regime the droplet radius decreases with decreasing continuous phase flow rate, satellites formed as a result of the droplet breakup process gravitate around the droplet until coalescence occurs.

The last two applications are devoted to the study of the influence of the external field (gravity) on multiphase flow and the position of the separation interface between the two immiscible fluids in contact. The hysteresis phenomenon has been investigated in a controlled manner, so that the experiments showed that the hysteresis cycle area is reduced when the microchannel is placed in a vertical position due to the stabilizing effect of gravity. When the viscosity ratio was high ($beta \approx 80$), gravity together with viscosity resulted in a smaller width of the oil phase when the channel was in lateral position with the oil phase down (UJ). When the viscosity ratio was unity ($beta \approx 1$), the oil phase had the smallest width when the channel was in vertical position. In this case gravity and density had a significant contribution on the interface position.

In the last part of the thesis, passive and active methods for separating cells and particles in microfluidic configurations were presented. Two Lab-on-a-chip devices were designed to separate red blood cells from circulating tumour cells in an alternating electric field using dielectrophoresis. The functionality of the devices is demonstrated with numerical simulations, the particles being directed to the corresponding output according to the sign of the dielectrophoretic force which is given by the Clausius-Mossotti factor (the factor that takes into account the relative permittivity of the medium and particles, the electrical conductivity of the medium and particles and the angular frequency).

**Important results:**

- Improving the manufacturing process of microchannels by flaring the inlet/outlet sections and creating microports;

- Determining the friction forces and pressures at the interface between two fluids by modeling the interface using the VOF method implemented in the ANSYS Fluent code;

- Enhancing mixing in microfluidic devices by depositing/growing nanostructures in microchannels, observed through vorticity distributions;

- Creating two benchmark applications for the flow of immiscible fluids in geometries with reduced dimensions, comparative study: experimental-numeric;

- Reducing hysteresis effect in multiphase flow in microchannels by investigating the hysteresis effect in a controlled manner and evaluating the influence of gravity on it;

- Modifying the position of the interface between two immiscible fluids in microfluidic devices using gravity (by changing the position of the microchannel with respect to the horizontal plane);

- Creating two Lab-on-a-chip devices for separating circulating tumor cells from healthy cells.


## Research perspectives

Interfacial phenomena have complex applications today, especially in the biotechnological and medical fields. In these applications, interfaces usually develop between viscoelastic fluids, the numerical modeling of which is difficult. Experimental studies are thus essential for analyzing the phenomena, especially if rigid or deformable cells are present in the flow.

The trifurcation channel, which has a small dimensional aspect but has a 1:4 ratio between the central inlet ($100\,\mu m$) and the main channel ($400\,\mu m$), is a representative geometry for testing viscoelastic fluids on a micro scale and verifying interface stability in contraction/extension flows [29], respectively in the presence of cells.

These studies are expected to be developed at the Laboratory for Micro- and Nano-Fluidics- L10 of the National Institute for Research and Development in Microtechnologies - IMT Bucharest.

The microchannel fabrication procedure influences the quality of the wall surface. Carbon nanomaterials have become extremely popular in the creation of Lab-on-a-chip devices, due to their electrical properties. Thus, depending on the device application, flow must be tested, as it has been shown that even a wall roughness of 400 nm can induce major changes in flow.

Regarding the fabrication procedure, a change from photolithography to laser technologies is also of interest. Of interest in these channels is the fact that the microchannel walls will be made exclusively from the same material (photosensitive glass), making it possible to compare the influence of contact angle on flow compared to PDMS channels.

Another aspect of interest is represented by the dimensional ratio of the microchannel. Thus, it is necessary to fabricate microfluidic devices with a high dimensional aspect to understand the influence that confinement has on flow and interfaces stability.

**The research perspectives are as follows:**

- Investigating the flow of viscoelastic fluids in channels with small dimensional aspect ratios;

- Continuing experimental investigations regarding the influence of external fields (especially electromagnetic fields) on the behavior of cells near fluid interfaces;

- Changing the fabrication procedure from photolithography to laser technologies and comparing the hydrodynamics of the two channels;

- Modifying the dimensional aspect ratio of the trifurcation and investigating its effect on flow stability.

# Bibliography

[1] S.S. Ahsan, A. Gumus, and D. Erickson. Redox mediated photocatalytic water-splitting in optofluidic microreactors. *Lab on a Chip*, 13(3):409–414, 2013.

[2] ANSYS Inc. Ansys fluent theory guide, r2. `https://ansyshelp.ansys.com/account/secured?returnurl=/Views/Secured/corp/v202/en/flu_th/flu_th.html`, 2020. Accesat: 12/07/2022.

[3] A.U.R. Aziz, C. Geng, M. Fu, X. Yu, K. Qin, and B. Liu. The role of microfluidics for organ on chip simulations. *Bioengineering*, 4(2):39, 2017.

[4] M.P. Borthakur, S. Succi, F. Sterpone, F. Pérot, A. Diko, and S. Melchionna. In-silico analysis of airflow dynamics and particle transport within a human nasal cavity. *Journal of computational science*, 54:101411, 2021.

[5] J. U. Brackbill, D. B. Kothe, and C. Zemach. A continuum method for modeling surface tension. *Journal of computational physics*, 100(2):335–354, 1992.

[6] C. Bălan. *Lecții de mecanica fluidelor*. Ed. Tehnică, București, 2003.

[7] I. Chakraborty, J. Ricouvier, P. Yazhgur, P. Tabeling, and A.M. Leshansky. Droplet generation at hele-shaw microfluidic t-junction. *Physics of Fluids*, 31(2):022010, 2019.

[8] Y.-C. Chang, T.Y. Hou, B. Merriman, and S. Osher. A level set formulation of eulerian interface capturing methods for incompressible fluid flows. *Journal of computational Physics*, 124(2):449–464, 1996.

[9] M. Chinaud, E.-P. Roumpea, and P. Angeli. Studies of plug formation in microchannel liquid–liquid flows using advanced particle image velocimetry techniques. *Experimental Thermal and Fluid Science*, 69:99–110, 2015.

[10] E. Chiriac, B. Adiaconiță, C. Pachiu, M. Avram, and C. Bălan. Micropiv on carbonic materials embedded in a microfluidic device. In *2021 International Semiconductor Conference (CAS)*, pages 169–172. IEEE, 2021.

[11] E. Chiriac, M. Avram, and C. Balan. Transition from threads to droplets in a microchannel for liquids with no viscosity contrast. In *2021 10th International Conference on ENERGY and ENVIRONMENT (CIEM)*, pages 1–4. IEEE, 2021.

[12] E. Chiriac, M. Avram, and C. Balan. Experimental and numerical investigation of hysteresis in multiphase flow in a microchannel. *UPB Scientific Bulletin, Series A: Applied Mathematics and Physics*, 84(3):191–200, 08 2022.

[13] E. Chiriac, M. Avram, and C. Balan. Investigation of multiphase flow in a trifurcation microchannel—a benchmark problem. *Micromachines*, 13(6):974, 2022.

[14] E. Chiriac, M. Avram, D. Broboana, and C. Balan. Interface evolution in a microchannel, an experimental and numerical study. In *2019 International Conference on ENERGY and ENVIRONMENT (CIEM)*, pages 219–223. IEEE, 2019.

[15] E. Chiriac, A.M. Bran, C. Voitincu, and C. Balan. Experimental validation of vof method in microchannel flows. In *2021 12th International Symposium on Advanced Topics in Electrical Engineering (ATEE)*, pages 1–4. IEEE, 2021.

[16] E. Chiriac, A.M. Bratu, M. Avram, and C. Bălan. Alcohol jets investigations in a microchannel in a viscous outer medium. In *IOP Conference Series: Earth and Environmental Science*, volume 664, page 012056. IOP Publishing, 2021.

[17] E. Chiriac, D. Broboana, M. Avram, and C. Balan. Comparative numerical study between openfoam and ansys fluent in a y-junction microchannel. In *2019 11th International Symposium on Advanced Topics in Electrical Engineering (ATEE)*, pages 1–4. IEEE, 2019.

[18] Comsol. Comsol multiphysics reference manual. `https://doc.comsol.com/5.5/doc/com.comsol.help.comsol/COMSOL_ReferenceManual.pdf`, 2019. Accesat: 31/08/2022.

[19] T.W. de Haas, H. Fadaei, U. Guerrero, and D. Sinton. Steam-on-a-chip for oil recovery: the role of alkaline additives in steam assisted gravity drainage. *Lab on a Chip*, 13(19):3832–3839, 2013.

[20] Y. Gao, K. Wu, Z. Chen, T. Zhou, J. Li, D. Feng, Y. Gao, and W. Tian. Effect of wetting hysteresis on fluid flow in shale oil reservoirs. *Energy & Fuels*, 35(15):12075–12082, 2021.

[21] A. Y. Gelfgat, A. L. Yarin, P. Z. Bar-Yoseph, M. D. Graham, and G. Bai. Numerical modeling of two-fluid taylor–couette flow with deformable capillary liquid–liquid interface. *Physics of Fluids*, 16(11):4066–4074, 2004.

[22] J.-M. Ghidaglia. Capillary forces: A volume formulation. *European Journal of Mechanics-B/Fluids*, 59:86–89, 2016.

[23] A. Hayen. Medical biostatistics (2nd edn). abhaya indrayan, chapman & hall/crc, boca raton, 2008. no. of pages: 824. price: $99.95. isbn10 1584888873, isbn 13: 9781584888871, 2010.

[24] C. W. Hirt and B. D. Nichols. Volume of fluid (vof) method for the dynamics of free boundaries. *Journal of computational physics*, 39(1):201–225, 1981.

[25] T. Holzmann. *Mathematics, Numerics, Derivations and OpenFOAM®*. 11 2019.

[26] D.Gh. Ionescu. *Introducere în mecanica fluidelor*. Ed. Tehnică, București, 2005.

[27] M. Kim, A. Sell, and D. Sinton. Aquifer-on-a-chip: understanding pore-scale salt precipitation dynamics during co 2 sequestration. *Lab on a Chip*, 13(13):2508–2518, 2013.

[28] E. Kjeang, R. Michel, D.A. Harrington, N. Djilali, and D. Sinton. A microfluidic fuel cell with flow-through porous electrodes. *Journal of the American Chemical Society*, 130(12):4000–4006, 2008.

[29] H.-C. Lee. A nonlinear weighted least-squares finite element method for the carreau–yasuda non-newtonian model. *Journal of Mathematical Analysis and Applications*, 432(2):844–861, 2015.

[30] H.-L. Li, H.-R. Liu, and H. Ding. A fully 3d simulation of fluid-structure interaction with dynamic wetting and contact angle hysteresis. *Journal of Computational Physics*, 420:109709, 2020.

[31] S. Liu, Y. Fu, C. Xiong, Z. Liu, L. Zheng, and F. Yan. Detection of bisphenol a using dna-functionalized graphene field effect transistors integrated in microfluidic systems. *ACS applied materials & interfaces*, 10(28):23522–23528, 2018.

[32] F. Mostowfi, S. Molla, and P. Tabeling. Determining phase diagrams of gas–liquid systems using a microfluidic pvt. *Lab on a Chip*, 12(21):4381–4387, 2012.

[33] S.A. Nabavi, G.T. Vladisavljević, M.V. Bandulasena, O. Arjmandi-Tash, and V. Manović. Prediction and control of drop formation modes in microfluidic generation of double emulsions by single-step emulsification. *Journal of colloid and interface science*, 505:315–324, 2017.

[34] C. Patrascu and C. Balan. The stabilizing effect of confinement on a liquid jet in a viscous outer fluid. *UPB Scientific Bulletin, Series A: Applied Mathematics and Physics*, 81:85–94, 01 2019.

[35] S.C. Pierobon, M.D. Ooms, and D. Sinton. Evanescent cultivation of photosynthetic bacteria on thin waveguides. *Journal of Micromechanics and Microengineering*, 24(4):045017, 2014.

[36] S. Popinet. Numerical models of surface tension. *Annual Review of Fluid Mechanics*, 50:49–75, 2018.

[37] P. Sajeesh and A. K. Sen. Particle separation and sorting in microfluidic devices: a review. *Microfluidics and nanofluidics*, 17(1):1–52, 2014.

[38] R. Scardovelli and S. Zaleski. Direct numerical simulation of free-surface and interfacial flow. *Annual review of fluid mechanics*, 31(1):567–603, 1999.

[39] A. Sciacchitano, B. Wieneke, and F. Scarano. Piv uncertainty quantification by image matching. *Measurement Science and Technology*, 24(4):045302, 2013.

[40] Z. Shi, Y. Zhang, M. Liu, D.A.H. Hanaor, and Y. Gan. Dynamic contact angle hysteresis in liquid bridges. *Colloids and Surfaces A: Physicochemical and Engineering Aspects*, 555:365–371, 2018.

[41] D. Sinton. Energy: the microfluidic frontier. *Lab on a Chip*, 14(17):3127–3134, 2014.

[42] M. Sommerfeld. Numerical methods for dispersed multiphase flows. In *Particles in flows*, pages 327–396. Springer, 2017.

[43] W. Song, H. Fadaei, and D. Sinton. Determination of dew point conditions for co2 with impurities using microfluidics. *Environmental science & technology*, 48(6):3567–3574, 2014.

[44] H.A. Stone, A. D. Stroock, and A. Ajdari. Engineering flows in small devices. *Annual review of fluid mechanics*, 36(1):381–411, 2004.

[45] M. Sussman, P. Smereka, and S. Osher. A level set approach for computing solutions to incompressible two-phase flow. *Journal of Computational physics*, 114(1):146–159, 1994.

[46] N.K. Thom, K. Yeung, M.B. Pillion, and S.T. Phillips. "fluidic batteries" as low-cost sources of power in paper-based microfluidic devices. *Lab on a Chip*, 12(10):1768–1770, 2012.

[47] V. Varmazyari, H. Habibiyan, H. Ghafoorifard, M. Ebrahimi, and S. Ghafouri-Fard. A dielectrophoresis-based microfluidic system having double-sided optimized 3d electrodes for label-free cancer cell separation with preserving cell viability. *Scientific reports*, 12(1):1–14, 2022.

[48] Z. Wang, K. Yi, Q. Lin, L. Yang, X. Chen, H. Chen, Y. Liu, and D. Wei. Free radical sensors based on inner-cutting graphene field-effect transistors. *Nature communications*, 10(1):1–10, 2019.

[49] W. Xin, T. Wu, T. Zou, Y. Wang, W. Jiang, F. Xing, J. Yang, and C. Guo. Ultrasensitive optical detection of water pressure in microfluidics using smart reduced graphene oxide glass. *Frontiers in chemistry*, 7:395, 2019.

[50] S. Zahedi, M. Kronbichler, and G. Kreiss. Spurious currents in finite element based level set methods for two-phase flow. *International Journal for Numerical Methods in Fluids*, 69(9):1433–1456, 2012.

[51] S. Zare Harofte, M. Soltani, S. Siavashy, and K. Raahemifar. Recent advances of utilizing artificial intelligence in lab on a chip for diagnosis and treatment. *Small*, page 2203169, 2022.